



# Experimental analysis of the multiaxial failure stress locus of commercially pure titanium at low and high rates of strain

Yuan Xu<sup>a</sup>, Maureen Aceves Lopez<sup>a</sup>, Junyi Zhou<sup>a</sup>, Lukasz Farbaniec<sup>a</sup>, Sophoclis Patsias<sup>b</sup>,  
Duncan Macdougall<sup>b</sup>, Julian Reed<sup>a</sup>, Nik Petrinic<sup>a</sup>, Daniel Eakins<sup>a</sup>, Clive Siviour<sup>a</sup>,  
Antonio Pellegrino<sup>a,\*</sup>

<sup>a</sup> Department of Engineering Science, University of Oxford, Parks Road, Oxford OX1 3PJ, United Kingdom

<sup>b</sup> Rolls-Royce PLC, PO Box 31, Derby, DE24 8BJ, United Kingdom

## ARTICLE INFO

### Keywords:

Split Hopkinson tension-torsion bar

Multiaxial failure

Failure stress envelope

Rate dependence

Commercially pure titanium

## ABSTRACT

The mechanical response and failure mechanism of commercially pure titanium subjected to combined tension-torsion loading are studied experimentally at strain rates ranging from  $10^{-3} \text{ s}^{-1}$  to  $10^3 \text{ s}^{-1}$ . A novel tension-torsion split Hopkinson bar (TTHB) equipped with a high speed camera was utilised during high-rate experiments, while quasi-static tests were conducted using a universal screw-driven machine. The multiaxial dynamic experiments demonstrate the ability of the developed TTHB apparatus to achieve synchronisation of longitudinal and torsional waves upon loading the specimen, to satisfy the dynamic equilibrium of the specimen and to attain constant strain rate loading. The failure envelope of commercially pure titanium was analysed over a wide range of stress states including pure torsion, shear-dominated combined tension-shear, tension-dominated combined tension-shear, and plain tension. The analyses of the loading paths show that these were nearly proportional in terms of strain. The multiaxial failure stress locus was constructed in the normal versus shear stress space from experiments conducted at low and high rates of strain.

The Drucker-Prager criterion was employed to approximate the failure envelope and to assess its rate sensitivity. The failure stress locus of commercially pure titanium and its rate dependence are reported for the first time. The TTHB apparatus developed allows the definition of the failure stress locus of aerospace materials directly from experiments and, therefore, the evaluation of the existing failure/yielding criteria.

## 1. Introduction

Titanium and its alloys have been used in a wide range of industrial applications from aerospace, biomedical, oil and gas, to marine industries [1–3], where their high strength-to-weight ratio, excellent chemical stability, and biocompatibility are of great advantage. Second only to the  $\alpha$ - $\beta$  alloy Ti-6Al-4 V that accounts for approximately 45% of the total titanium production, commercially pure titanium (CP-Ti) comprises approximately 30% of the production. As a load-bearing material for structural components in applications such as joint replacement systems, high pressure compressors, ducting for environmental control systems, titanium typically undergoes combined loads at high rates of strain due to the complex working conditions [1,2,4–6]. The mechanical behaviour of titanium subjected to high-rate multiaxial loads is not fully understood yet because of the intrinsic microstructural

complexity of the material and the difficulties in laboratory experimentation and instrumentation. Knowledge of the multiaxial response and failure mechanism of titanium at high strain rate has begun to draw increasing attention, driven by a variety of advanced engineering applications, but also by the development of accurate constitutive models and failure criteria for these materials.

The split Hopkinson pressure bar (SHPB) [7], also called Kolsky bar [8], has been, up to date, the most popular technique to characterise the dynamic response of the vast majority of materials at strain rates ranging from  $10^1$  to  $10^4 \text{ s}^{-1}$  [9,10]. Since its incipience, this technique has been extensively developed and one significant modification has been the split Hopkinson tension bar [11]. The majority of the available studies on the mechanical response of CP-Ti at high strain rate focus on uniaxial compression and uniaxial tension loading.

Previous research on the dynamic compressive behaviours has

\* Corresponding author.

E-mail address: [antonio.pellegrino@eng.ox.ac.uk](mailto:antonio.pellegrino@eng.ox.ac.uk) (A. Pellegrino).

<https://doi.org/10.1016/j.ijimpeng.2022.104341>

Received 6 October 2021; Received in revised form 13 January 2022; Accepted 28 July 2022

Available online 30 July 2022

0734-743X/© 2022 The Author(s). Published by Elsevier Ltd. This is an open access article under the CC BY license (<http://creativecommons.org/licenses/by/4.0/>).

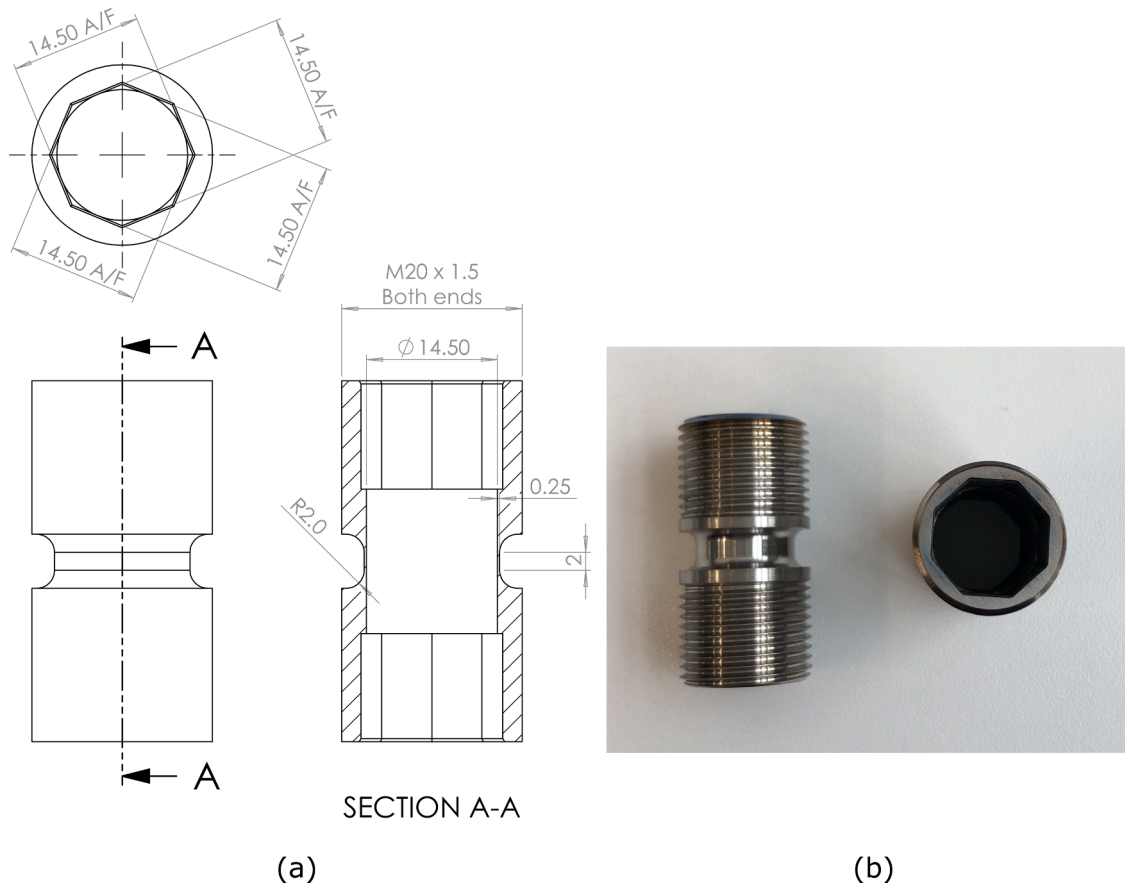


Fig. 1. Specimen used in combined tension-torsion experiments: (a) geometry and dimensions; (b) CP-Ti specimen.

shown pronounced strain rate sensitivity of the flow stress which is associated with the dislocation density. Chichili et al. [12] measured the stress-strain curves of  $\alpha$ -titanium under compression at strain rates ranging from  $10^{-5} \text{ s}^{-1}$  to  $10^4 \text{ s}^{-1}$  and concluded that the effective flow stress increased with the strain rate and that the material appeared to be more strain rate sensitive at the highest strain rates region; at low strain rates and strain, the deformation was mainly caused by dislocation with few twins, while the twinning density increased at high strain rates. Gurao et al. [13] investigated the compressive behaviour of commercially pure titanium with four different initial orientations at strain rates between  $3 \times 10^{-4} \text{ s}^{-1}$  and  $1.5 \times 10^3 \text{ s}^{-1}$  and built a viscoelastic model able to capture texture evolution, stress-strain response, and twinning progression. The dynamic compressive behaviour of an  $\alpha$ -titanium characterised by higher purity at strain rates up to  $3000 \text{ s}^{-1}$  was measured in another study [14]. Kailas et al. [15,16] studied the plastic flow of  $\alpha$ -titanium and observed significant adiabatic shear banding in the specimen when it deformed in compression at strain rates in the region of  $100 \text{ s}^{-1}$  and temperatures between 298 K and 473 K. Nemat-Nasser et al. [17] investigated the compressive behaviour of pure titanium at a wider range of strain rates and temperatures reaching consistent conclusions.

Considerable efforts have been made to investigate the strain rate and temperature effects on the flow stress and deformation mechanism of CP-Ti under dynamic tensile loading. Harding et al. [18] measured the tensile stress-strain curves of  $\alpha$ -titanium at various temperatures (77–298 K) and strain rates ( $10^{-3}$ – $1.5 \times 10^3 \text{ s}^{-1}$ ) using an Instron screw-driven tensometer, a hydraulic machine, and a drop-weight impact machine. The rate sensitivity of the flow stress was found to increase with the increasing strain rate above  $50 \text{ s}^{-1}$  at all temperatures. Huang et al. [19] developed a high temperature tensile Hopkinson bar and examined the dynamic properties of commercially pure titanium at

strain rates ranging from  $3 \times 10^2 \text{ s}^{-1}$  to  $1.4 \times 10^3 \text{ s}^{-1}$ , at the temperature range of 298–973 K. It was found that the flow stress, yield stress and ultimate stress increase slightly with the increasing strain rate at indicated temperatures, which was explained through optical metallography observations showing that the density of deformation twinning increased with the increasing strain rate. Similar results were found in [20], in which the tensile behaviour of CP-Ti was studied under moderately high strain rate ( $200$ – $1000 \text{ s}^{-1}$ ) using a pendulum-driven Hopkinson bar.

Few studies investigated the dynamic shear response of CP-Ti. A modified split Hopkinson torsion bar apparatus was employed to test  $\alpha$ -titanium tubular specimens over a wide range of shear strain rates up to  $2 \times 10^3 \text{ s}^{-1}$  [21]; similar to other studies, an evident rate sensitivity in the shear stress-strain curves was reported and the yield stress at the strain rate of  $1250 \text{ s}^{-1}$  was found to be more than twice the quasi-static value. Shear stress-strain curves of CP-Ti were measured at a strain rate of about  $10^5 \text{ s}^{-1}$  using pressure-shear plate techniques [12], in which an obvious rate-sensitivity was detected.

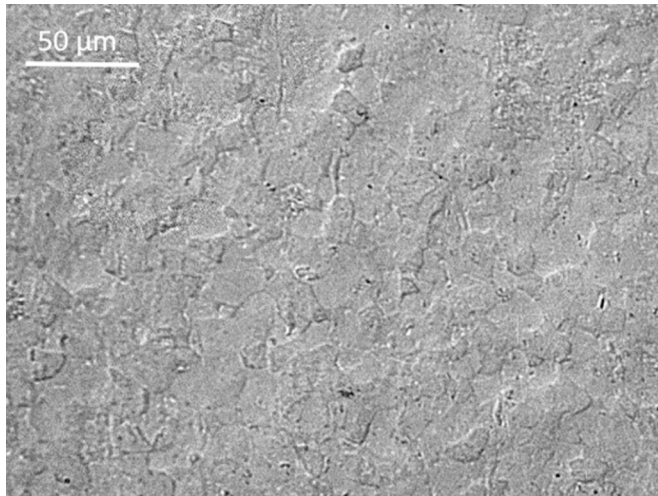
Very limited work is found in the literature about CP-Ti subjected to combined tension-torsion loading. Randall and Campbell [22] applied combined tension/torsion loading on pure titanium over a limited range of moderate strain rates using a biaxial hydraulic testing machine. Chen et al. [23] studied the deformation process of pure titanium under several combinations of tension-torsion loading at quasi-static rate range. Their study focused on the microstructure and fracture morphology of the specimen; thus, no stress-strain relation was reported. At the best of our knowledge, no previous studies report the mechanical behaviour of pure titanium subjected to combined loading at high strain rates.

Therefore, the aim of the present work is to investigate the multiaxial failure of CP-Ti subjected to different combinations of tension and

**Table 1**

Impurity composition (wt%) of the commercially pure titanium under investigation.

Fe	C	N	H	O
0.4	0.08	0.03	0.016	0.175

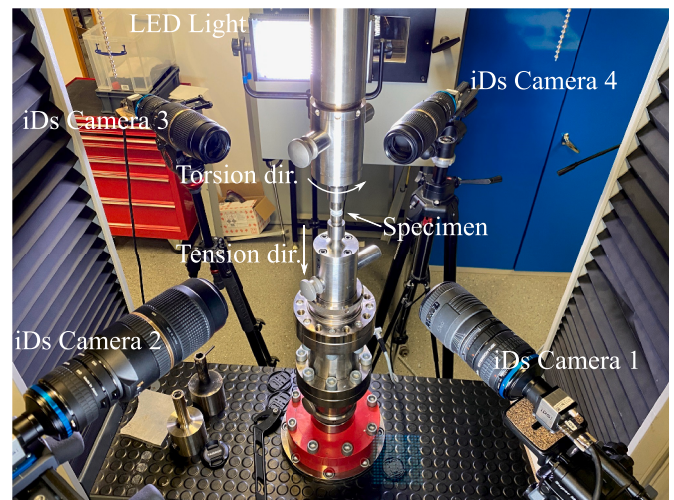
**Fig. 2.** Initial microstructure of the CP Ti grade 4 investigated.

torsion loads at quasi-static and dynamic strain rates and to analyse the failure stress locus and its strain rate sensitivity. A novel split tension-torsion Hopkinson bar (TTHB), equipped with high-speed cameras, was employed in the high-rate experiments. Strains were measured by means of digital image correlation (DIC) techniques. The material and specimen design are briefly introduced in Section 2, while Section 3 describes the experimental methods used in the quasi-static and high-rate tests. Results are discussed in Section 4. Section 5 summarises the whole study.

## 2. Specimen and material

Thin-walled tubular specimens of geometry shown in Fig. 1 were manufactured from commercially pure titanium grade 4 (CP Ti grade 4) to characterise its mechanical response under different stress states including tension, torsion, and their arbitrary combinations. Table 1 presents the chemical composition of the material. The material was supplied in the form of hot rolled rods of diameter equal to 20 mm and length equal to 1000 mm. The samples were manufactured by means of electro erosion, turning and milling such a way that the axis of the samples was collinear to the axis of the rod. A micrograph of the material investigated in as received conditions is shown in Fig. 2. The average grain size was estimated to be 18  $\mu\text{m}$ , which is in the range between 10  $\mu\text{m}$  and 25  $\mu\text{m}$  of the typical average grain sizes reported in the literature for CP Ti grade 4 hot rolled bars in as received conditions [24,25]. Both ends of the specimen are specially shaped with an octagonal slot and external threads to enable the transmission of both torque and axial load throughout the specimen. The input and output bars are provided with octagonal studs corresponding to the slots in the specimen and are connected to the specimen by means of threaded collars.

The dimensions of the sample were selected to promote the attainment of an approximately uniform distribution of stresses along the gauge length and across the wall thickness and to facilitate the achievement of dynamic equilibrium conditions during dynamic tension-torsion loading. Similar specimen geometries were successfully adopted in [26] on 0.33 mm thickness aluminium samples, in [27] where a wall thickness equal to 0.3 mm was used for high-rate torsion

**Fig. 3.** Quasi-static testing setup.

experiments on Ti6Al4V, and in [28] where repeatable results at three different strain rates were obtained on Ti3Al2.5 V using a wall thickness of 0.3 mm. The specimen geometry used in this work introduced a gradual transition between specimen gauge section and shoulders to avoid stress concentrations during tensile loading. The wall thickness was reduced to 0.25 mm to extend the range of strain rates achievable during combined tension-torsion loading, particularly when tension predominates over shear.

## 3. Experimental methods

### 3.1. Quasi-static tests

Quasi-static (QS) experiments were conducted in laboratory conditions using a Zwick/Roell Z250 screw-driven universal testing machine (Fig. 3). The loads were applied under displacement control at a speed of  $2 \times 10^{-3}$  mm/s in tension and  $0.02^\circ/\text{s}$  in torsion. Four iDs<sup>1</sup> UEye USB 3.0 Cameras were set up, as shown in Fig. 3, and synchronised to video-record the macroscopic deformation mechanism and to capture the failure initiation of the cylindrical specimens. Pictures were taken at a frame rate of 1 fps via a CMOS sensor with a resolution of  $2456 \times 2054$  pixels. A fine grey-scale speckle pattern was applied to the surface of the specimen to acquire full-field tensile and shear displacement by means of DIC analysis of the high-resolution video footage. The quality of the speckle pattern was verified using the mean intensity gradient (MIG) [29,30]. A MIG value of 44.6 was calculated for the speckled region of interest for the experiment labelled as #QS5 shown in Fig. 9b. A mean bias error of displacement of less than 1% was reported for MIG values greater than 20 [29]. The applied force and torque were recorded via the respective resistive load cells,<sup>2</sup> while the history of the axial and shear strain within the gauge section of the specimen were measured from DIC using commercial software LaVision Davis.

### 3.2. High strain rate tests

High-rate (HR) experiments were accomplished in laboratory conditions using a specially designed and built TTHB system. The testing setup is presented in Fig. 4, while the schematic is illustrated in Fig. 5. The TTHB system consists of an input bar, an output bar, a specimen sandwiched in between, a rapid release clamp assembly, a pre-tension loading unit (linear actuator), a pre-torsion loading unit (rotary

<sup>1</sup> IDS Image Development Systems GmbH

<sup>2</sup> Zwick XForce 100 kN, Zwick torque transducer 1000 Nm



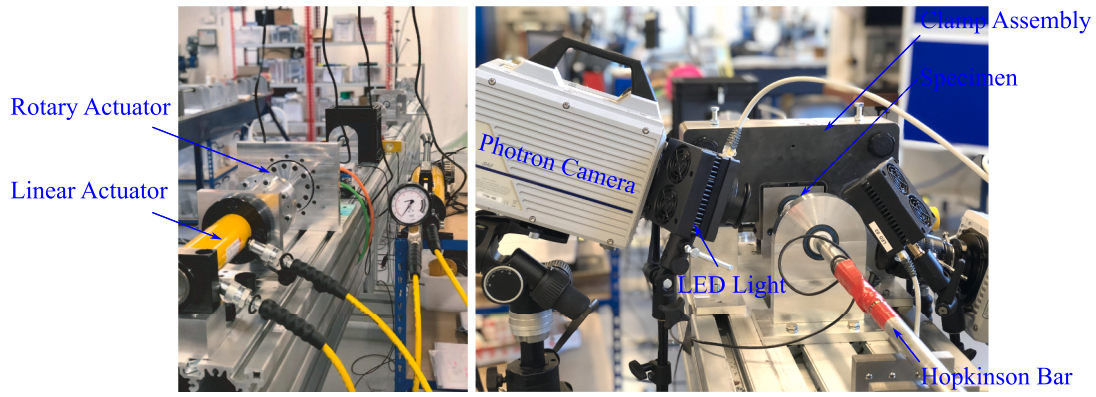


Fig. 4. High strain rate testing setup: split Hopkinson tension-torsion bar (TTHB).

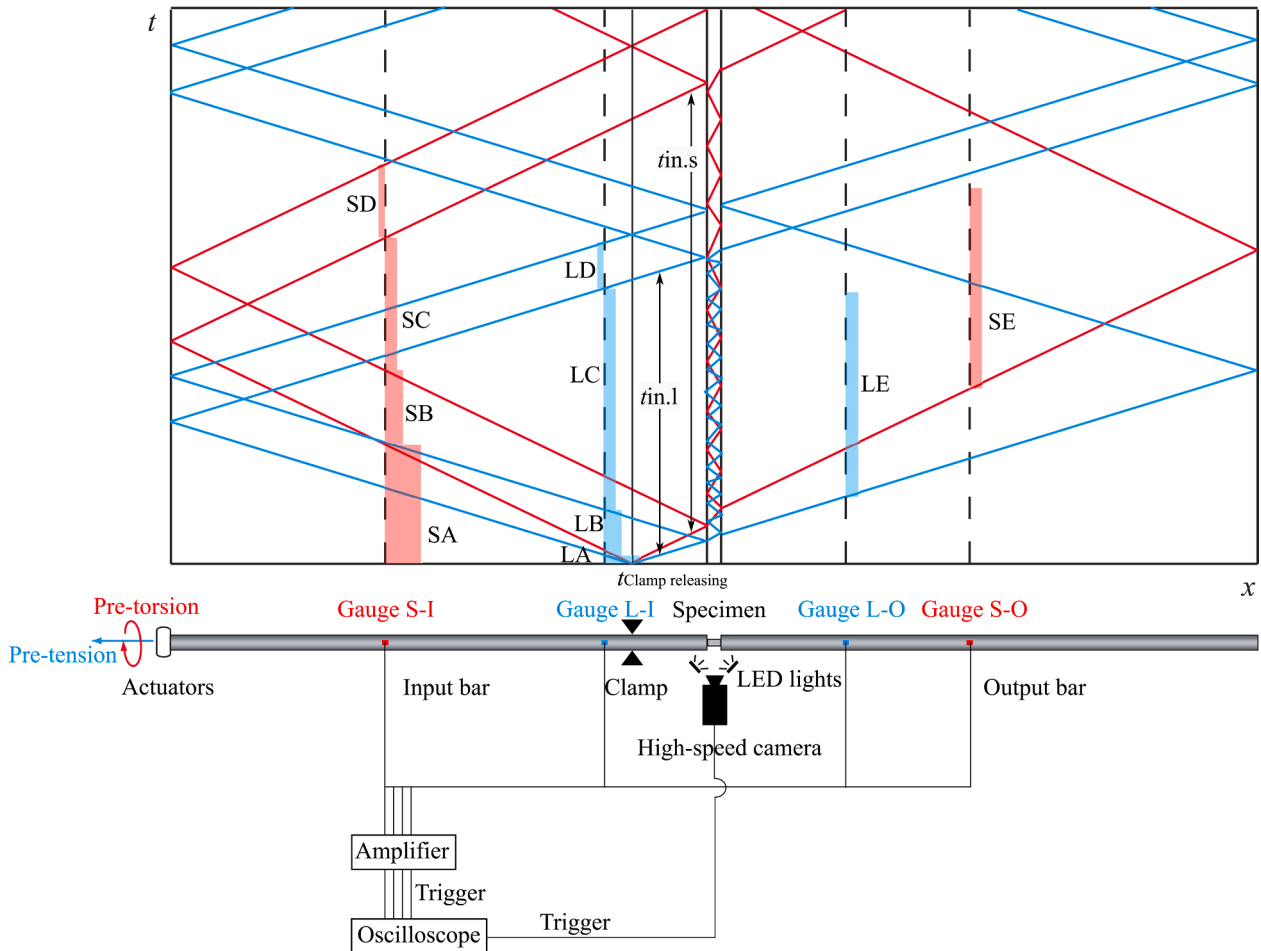


Fig. 5. Schematic of the TTHB system and  $x$ - $t$  (Lagrange) diagram of wave propagation.

actuator), and a data acquisition system. Both the input bar and the output bar are made of Al 7075-T6, with a length of 2500 mm and diameter of 20 mm. In a typical dynamic tension-torsion loading experiment, the input bar is mechanically clamped at a certain distance from the bar-specimen interface, while the opposite end of the bar is driven to extend until reaching a prescribed force and to rotate until exerting a desired torque. An amount of tensile and torsional strain energies is therefore stored in the clamped section of the input bar. The output bar is instead free to slide along and rotate about its axis. The stored tensile and torsional energies are released in the form of longitudinal and torsional waves by inducing failure of a notched aluminium

pin that keeps the clamp tight to the bar. The resulting shear and axial waves propagate along the bar in both forward and backward directions from the clamp. At this instant, a dynamic combined tension-torsion test is initiated. Similar store-and-release systems to generate a pulse in a split Hopkinson bar system have been used in Hopkinson torsion bar techniques [31–33]. In the case of high-rate pure tension or pure torsion loading using the TTHB used for this research, only tensile or torsional energy is stored initially in the input bar. Thus either tensile wave or shear wave will be generated upon the rapid release of the clamp.

The data acquisition system included a set of longitudinal and shears strain gauges on both the input and the output bars, and a high-speed



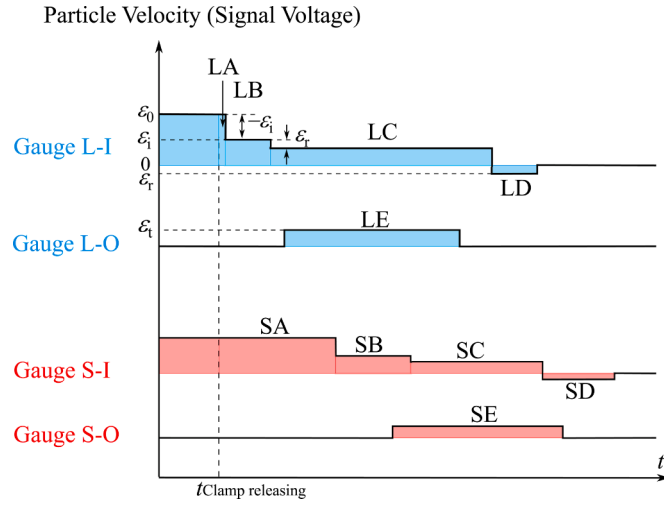


Fig. 6. Theoretical  $v$ - $t$  diagram of the wave propagation recorded from four strain gauge channels.

Photron SA-5 Camera focused on the specimen. The tensile and shear strain gauges on the input bar were located 180 mm and 1063 mm away from the input end of the specimen respectively, while the distances between the output end of the specimen and the tensile and shear strain gauges on the output bar were 345 mm and 575 mm, correspondingly. The strain gauges were located in positions such that the propagation of the tensile and torsional waves in both the input and output bars can be recorded without superposition with the waves reflected from the far end of the bars prior to the failure of the specimen. The history of the loads was calculated via the wave analysis based on D'Alembert's solution [34]. The high-speed video footage was recorded at a frame rate of  $10^5$  fps with a resolution of  $256 \times 232$  pixels. A fine grey-scale speckle pattern was applied to the surface of the specimen to facilitate DIC analysis to determine the full-field displacement, from which the time history of the overall engineering tensile and shear strain within the gauge section can be calculated. The MIG value [29,30] of 20.2 was calculated in the speckled region of interest for the experiment #HR6 shown in Fig. 13b.

The propagation of the longitudinal and shear waves is illustrated via the  $x$ - $t$  diagram and the  $v$ - $t$  diagram in Figs. 5 and 6, respectively. The lines and shades in blue denote the longitudinal wave, whereas red ones the shear wave. The longitudinal wave is taken as an example as follows to elaborate the wave generation and propagation when using the above-mentioned clamping-releasing method: (a) After the input bar is clamped at a designated position and then loaded at the far end, the clamped section of the input bar is in a uniaxial tensile stress state  $\varepsilon_0$  (state LA in Figs. 5 and 6), measured by the longitudinal strain gauge L-I; (b) Upon the sudden release of the clamp, the stored tensile energy is released and propagates as two longitudinal waves in opposite directions from the clamp, at a wave speed  $c_l = \sqrt{E/\rho}$ , where  $E$  and  $\rho$  are the Young's modulus and density of the bar, respectively. Given the law of conservation of momentum, the two waves have the same absolute amplitude corresponding to half of the stored energy but have opposite signs. The one that travels towards the pre-loading units, namely the released compressive wave  $-\varepsilon_i$ , counteracts half of the initial tensile stress. This state corresponds to LB, i.e.,  $\varepsilon_0 + (-\varepsilon_i)$  in Figs. 5 and 6; (c) The other one, that propagates towards the specimen is by convention called the input tensile wave  $\varepsilon_i$ . This will, at the bar-specimen interface, partially transmit into the output bar as the output tensile wave  $\varepsilon_t$  (state LE in Figs. 5 and 6) and partially reflect back into the input bar as the reflected compressive wave  $\varepsilon_r$ , due to the impedance mismatch at the interface between input bar and specimen and to the interaction of the waves with the sample; (d) When the reflected wave  $\varepsilon_r$  travels back into the initially clamped section and superposes onto the released

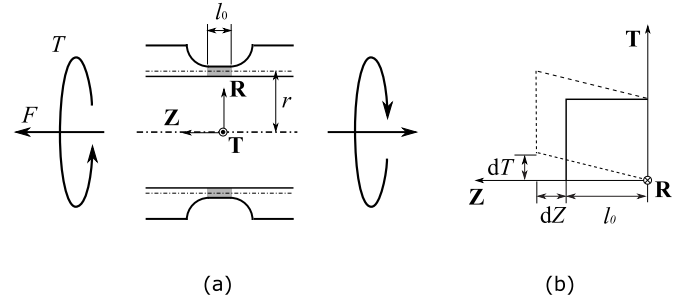


Fig. 7. (a) A schematic of the gauge section of the thin-walled tube specimen subjected to combined tension-torsion loading, and (b) the induced stretching and shearing at a material point as a result of a normal displacement  $dZ$  and a shear displacement  $dT$ .

compressive wave  $-\varepsilon_i$ , the state of the input bar at Gauge L-I changes from LB to LC (Figs. 5 and 6). It is noted that, as  $\varepsilon_i = \varepsilon_0 / 2$ ; the state LC in Fig. 6 represents the superposition of the effective input wave and the effective reflected wave ( $\varepsilon_0 - \varepsilon_i + \varepsilon_r = \varepsilon_i + \varepsilon_r$ ) as in a three-wave analysis of a conventional Hopkinson bar experiment. The achievement of dynamic equilibrium conditions can hence be evaluated by comparing the state LC ( $\varepsilon_i + \varepsilon_r$ ) read off from gauge L-I and the state LE ( $\varepsilon_t$ ) from gauge L-O; (e) Subsequently, due to the sufficiently large mechanical impedance of the pre-loading units, the released compressive wave  $-\varepsilon_i$  reflects back at the bar end, remaining a compressive wave of amplitude  $-\varepsilon_i$ . This wave further counterbalances the initial tensile stress state to zero as it propagates from the bar end. In the example shown in Fig. 5, where the clamp is located near the specimen and the strain gauge is far from the pre-loading unit, the amplitude of the state LD is equal to the magnitude of the reflected wave  $\varepsilon_r$ ; (f) The initially stored tensile energy is not completely counterbalanced until the reflected compressive wave  $-\varepsilon_i$  travels back to the clamp. Hence, the duration of the incident longitudinal wave that effectively interacts with the specimen is the period  $t_{in,l}$  for which the wave travels back and forth the distance between the clamp and the pre-loading unit.

Likewise, the torsional wave is generated via the rapid release of the stored torsional strain energy but propagates at a wave speed  $c_s = \sqrt{G/\rho}$ , where  $G$  is the shear modulus of the bar. The theoretical duration of the incident shear wave is  $t_{in,s}$  equal to the time required to the elastic shear wave to travel back and forth the distance between the clamp and the pre-loading unit. In the presented TTHB system, a single clamp is employed to initiate simultaneously both the tensile and torsional waves. The wave propagation velocity of the shear wave is lower than the longitudinal wave speed. To minimise the difference in time between the instants the longitudinal and shear incident waves reach the specimen, the clamp assembly is positioned in immediate proximity to the sample, 40 mm away from the interface between the specimen and the input bar. More details on the working principle and the calculation of stored loads can be found in [35].

### 3.3. Evaluation of stress and strain

A cross-section of the axisymmetric specimen geometry along the axial direction is illustrated in Fig. 7a, where a cylindrical coordinate system  $RTZ$  is introduced. Given the force  $F$  and torque  $T$  the specimen is enduring, the average engineering direct stress  $\sigma$  ( $\sigma_{zz}$ ) and shear stress  $\tau$  ( $\sigma_{zt}$ ) on the cross-section of the thin-walled tube are calculated, by assuming homogeneous stress distribution, as Eqs. (1) and 2:

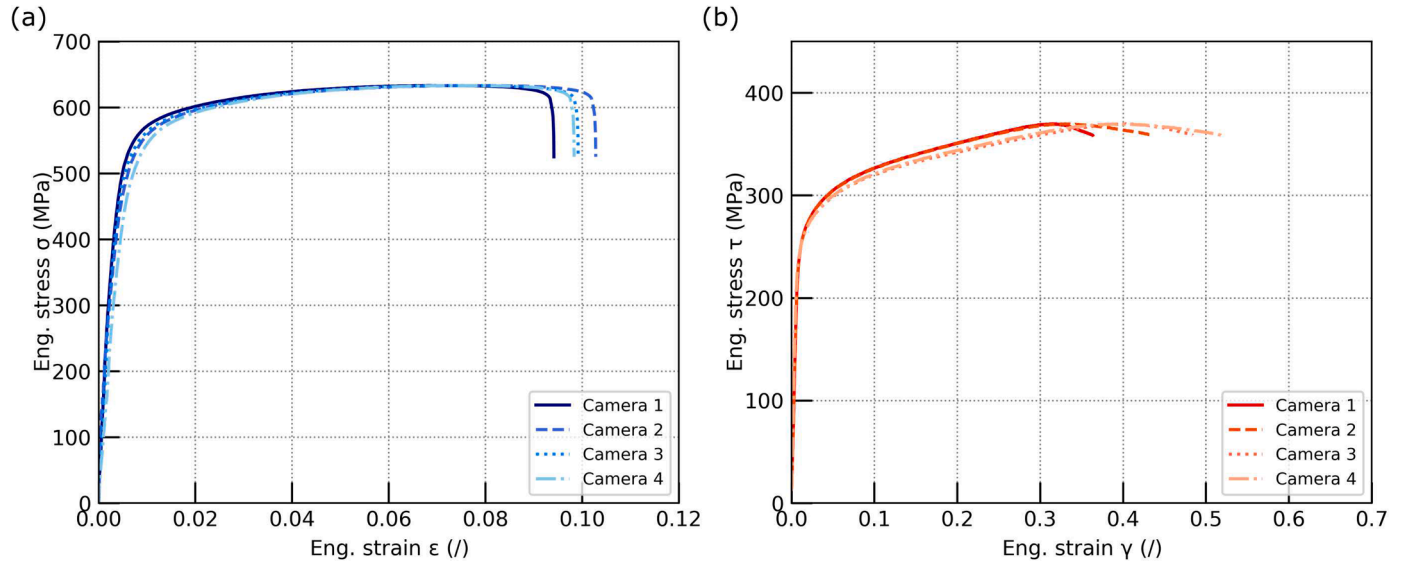
$$\sigma = \frac{F}{A} \quad (1)$$

$$\tau = \frac{Tr}{J} \quad (2)$$

**Table 2**

Summary of experiments conducted in this study.

Type of test	Specimen #	Biaxial loading angle °	Strain rate $s^{-1}$		Ultimate stress MPa		Percent elongation %		$\Delta t$ μs
			Tension	Shear	Tension	Shear	Tension	Shear	
Tension	QS1	90.0	0.001		589.44		7.95		
	QS2	90.0	0.001		633.20		9.42		
	HR1	90.0	113		746.62		9.53		
Torsion	QS3	0.0		0.001		369.69		36.35	
	QS4	0.0		0.001		324.23		37.18	
	HR2	0.0		934		576.26		40.18	
	HR3	0.0		1380		558.70		28.24	
Combined tension-torsion	QS5	49.5	0.001	0.001	488.51	240.49	11.04	19.64	
	HR4	42.5	420	649	760.39	456.06	8.77	12.99	20
	HR5	40.2	253	696	695.75	450.63	8.69	14.83	24
	HR6	39.6	485	890	572.24	399.16	10.58	20.05	20
	HR7	20.1	133	460	317.61	500.13	8.22	25.40	22
	HR8	18.3	116	300	268.94	469.56	4.54	14.80	20

**Fig. 8.** Stress-strain relationships at quasi-static rate in (a) tension (#QS2,  $\beta = 90.0^\circ$ ), and (b) torsion (#QS3,  $\beta = 0.0^\circ$ ).

where,  $A$ ,  $r$ , and  $J$  denote the cross-section area, mean radius, and polar moment of inertia of the gauge region of the thin-walled tube, respectively.

The biaxial loading angle  $\beta$  (Eq. (3)), defined as the ratio of the direct stress  $\sigma$  over the shear stress  $\tau$  multiplied by  $\sqrt{3}$ , is introduced to describe the contribution of tension and torsion to the combined loads. In this study, the biaxial loading angle will be limited to the interval  $0^\circ \leq \beta \leq 90^\circ$ , where  $\beta = 0^\circ$  corresponds to torsion loading,  $\beta = 90^\circ$  tension loading, and  $0^\circ < \beta < 90^\circ$  any arbitrary combination of tension and torsion.

$$\tan \beta = \frac{\sigma}{\sqrt{3}\tau} \quad (3)$$

A planar section that is initially coplanar with the  $\mathbf{Z}$ - $\mathbf{R}$  plane will deform in the  $\mathbf{Z}$ - $\mathbf{T}$  space with a normal displacement  $dZ$  and a shear displacement  $dT$ , illustrated as combined stretching and shearing at a material point in Fig. 7b. The nominal tensile strain  $\varepsilon$  ( $\varepsilon_{zz}$ ) and the nominal shear strain  $\gamma$  ( $\gamma_{zt}$ ) can be determined as:

$$\varepsilon = \frac{dZ}{l_0} \quad (4)$$

$$\gamma = \frac{dT}{l_0} \quad (5)$$

where,  $l_0$  represents the initial length of the gauge section.

#### 4. Results and discussion

The multiaxial deformation and failure of commercially pure titanium obtained from the quasi-static and dynamic tension-torsion experiments are presented in this section. A summary of the imposed strain rates and the mechanical characteristics measured in different loading cases is detailed in Table 2. The experiments conducted in quasi-static and dynamic loading regimes in this study cover a wide range of stress states ranging from pure shear ( $\beta = 0^\circ$ ) to pure tension ( $\beta = 90^\circ$ ), with shear-dominated and tension-dominated combined tension-torsion in between. It is noted that the wave synchronisation is evaluated by comparing the instants at which the incident longitudinal and shear waves reached their nominal amplitudes ( $\Delta t$  in Table 2).

##### 4.1. Quasi-static response

Quasi-static tension and torsion experiments serve as a reference to probe the effect of stress triaxiality and strain rate sensitivity on the mechanical response of commercially pure titanium. Representative nominal stress-strain curves are presented in Fig. 8. The four curves in each plot are associated to different strain histories measured from four cameras focusing on distinct regions of the specimen gauge length (see Fig. 3). Zhang et al. reported that the error in measuring the shear strain

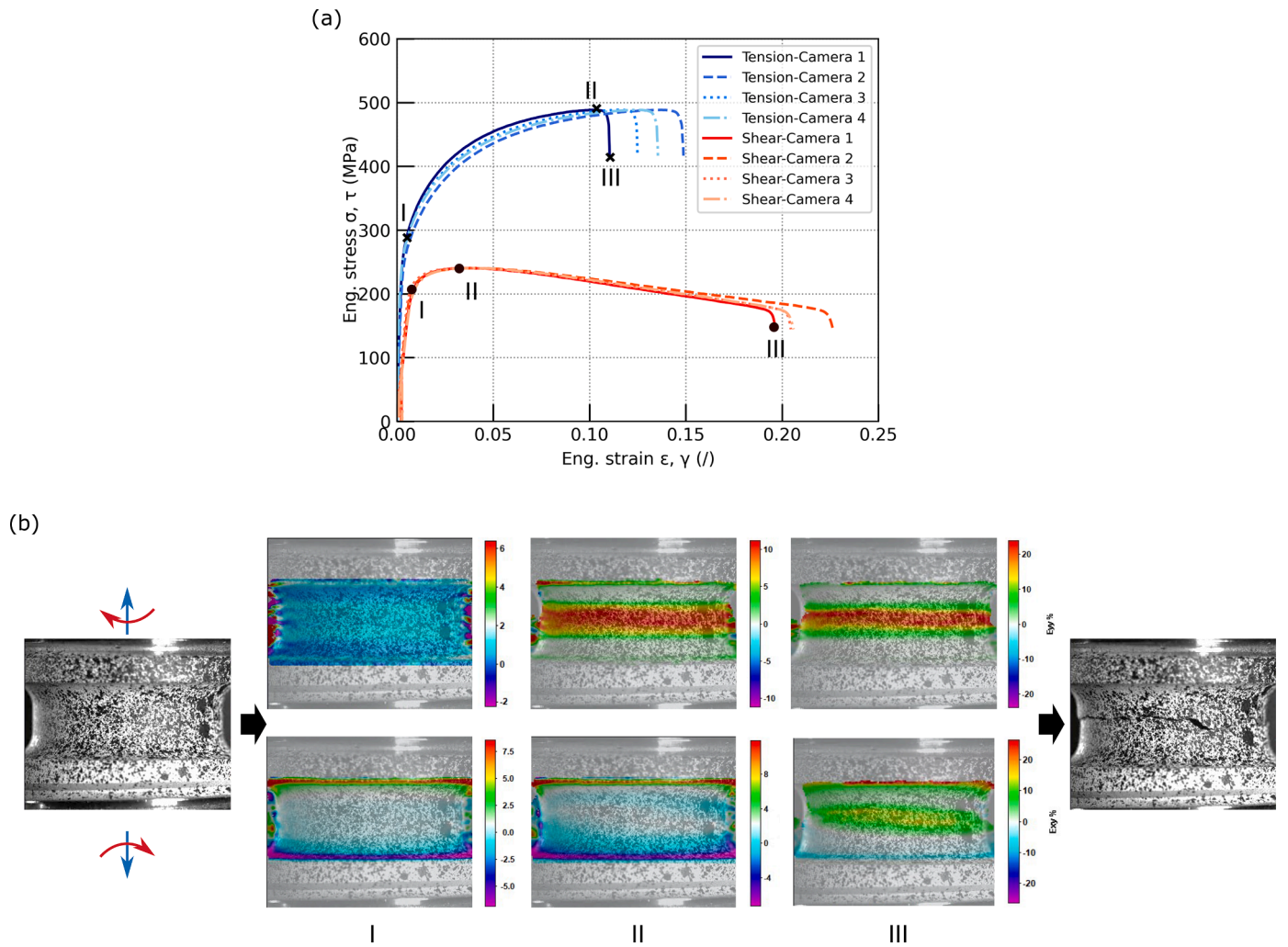


**Fig. 9.** (a) Stress versus strain curves of CP-Ti subjected to combined tension-torsion loading at quasi-static rate (#QS5,  $\beta = 49.5^\circ$ ) and (b) progressive deformation and failure.

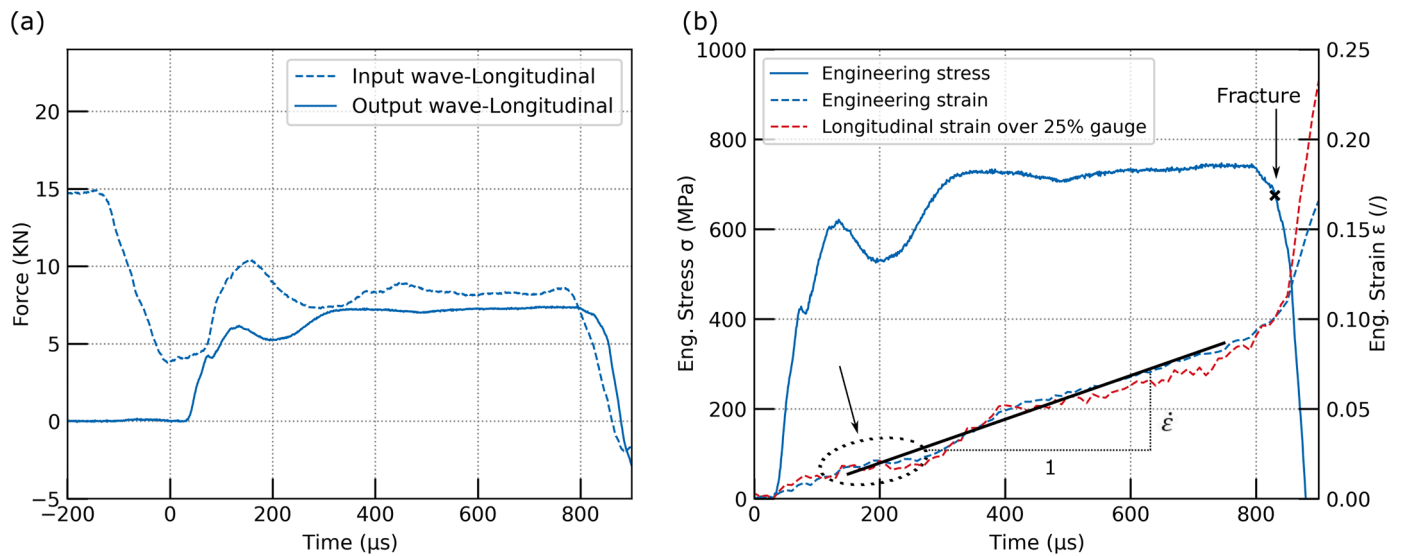


**Fig. 10.** High-rate responses from a tension loading experiment (#HR1,  $\beta = 90.0^\circ$ ): (a) assessment of dynamic equilibrium and (b) time histories of engineering direct stress, engineering direct strain and local longitudinal strain over 25% of the gauge length around the centre of the sample.



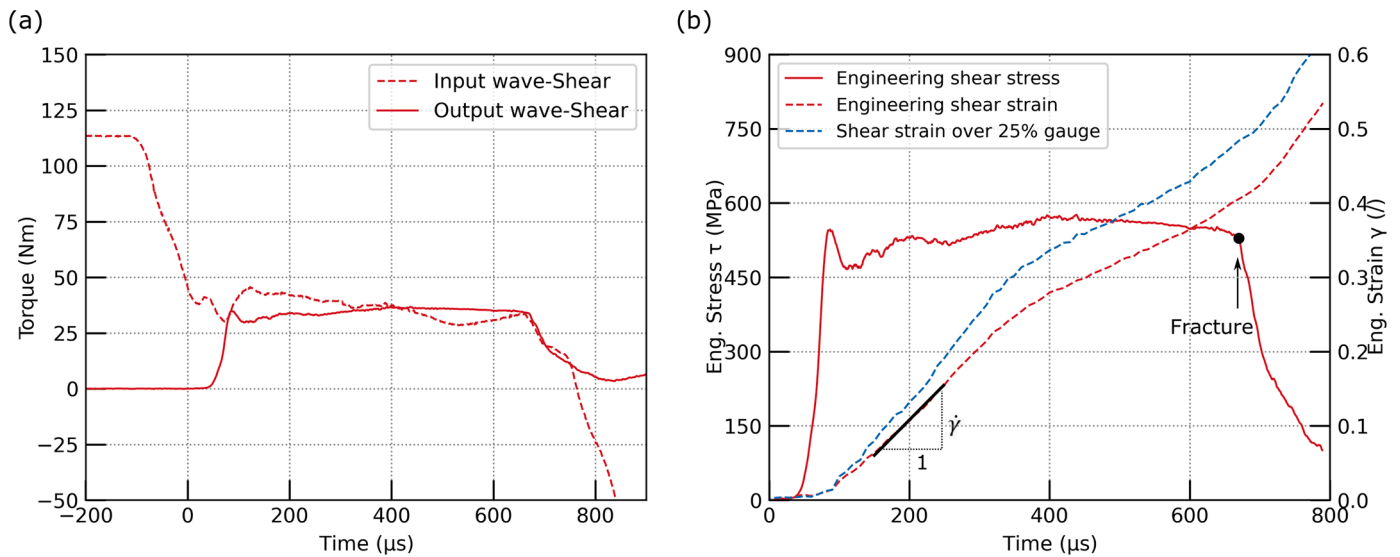


**Fig. 11.** High-rate responses from torsion loading test (#HR2,  $\beta = 0.0^\circ$ ): (a) assessment of dynamic equilibrium and (b) time histories of shear stress, engineering shear strain and local shear strain over 25% of the gauge length around the centre of the sample.

using 2D DIC analysis is negligible when  $\gamma$  is lower than 0.75 radians [36]. As the maximum engineering shear strain measured in this study did not reach 0.75, shear strains were measured using 2D DIC analysis. Repeatable strain histories were observed during elastic deformation and strain hardening region for both  $\beta = 90.0^\circ$  and  $\beta = 0.0^\circ$ . The tensile flow curves displayed strain hardening up to an axial strain equal to 6%, followed by saturation of the flow stress (no strain hardening) and fracture right after the ultimate stress strength point, 633 MPa, without obvious necking. The average measured strain to failure is 9.42%. The same trend was observed in all repetitions of the tensile tests. The stress strain curves measured in torsion showed strain hardening up to an engineering shear strain  $\gamma$  equal to 0.32 radians followed by a drop in stress and failure of the specimen. The measured ultimate shear stress equal to 370 MPa corresponds to a von Mises equivalent stress of 640 MPa, which is comparable with the measured ultimate tensile strength.

The nominal stress-strain curves measured during combined tension-torsion loading experiments are shown in Fig. 9a. The axial flow stress displays significant strain hardening up to failure, while the shear flow curves show negligible strain hardening with the specimen undergoing significant strain localisation after the ultimate shear point. Compared with the behaviours under tension or torsion loading, the ultimate strength and failure strain measured under combined loading appear to be in between the ones measured in uniaxial tension and torsion, due to the simultaneous presence of both direct and shear stresses. The ultimate tensile stress decreased while the percent elongation increased slightly. Correspondingly, a noticeable decrease was observed on both the ultimate shear stress and the shear strain to failure. The full field axial and shear strains across the gauge region are presented in Fig. 9b. Three identifiable loading stages are shown: (I) the yielding point; (II) the ultimate point; and (III) the fracture onset, as marked in Fig. 9a. It is noted that the ultimate point is not simultaneous under combined loading conditions. The contour maps indicate the uniformity of the strain field along the circumferential direction up to fracture initiation. The final crack was located near the middle plane in the gauge section.

#### 4.2. High strain rate response

The high-rate behaviour under tension loading is presented in Fig. 10. Fig. 10a reports the comparison of the calculated force histories at the input and output sides of the specimen. The recorded longitudinal wave signals have been shifted to the bar-specimen interface known the positions of the strain gauges and the longitudinal wave speed of the bar

material. In this shifted time, the drop in the initial level of the input wave thus indicates the instant at which the incident wave started loading the specimen. Thereafter, the input wave oscillated and approached a constant amplitude. As illustrated by Figs. 5, 6 in Section 3.2, the force imposed at the incident side of the specimen can be calculated as the sum of the incident and reflected waves and measured directly due to the convenient location of the longitudinal strain gauge L-I. The recorded output stress wave described the time history of the force acting on the output side of the specimen.

It is observed that the input force oscillates significantly during the initial phases of loading between 0 and 200  $\mu\text{s}$ , deviating substantially from the output force. This initial oscillation is plausibly due to a not smooth release of the clamp. The early diversion from dynamic equilibrium may be attributed to some initial slack in the mechanical connections between collars and bars, and between collars and specimen. After 200  $\mu\text{s}$  the oscillations in the force histories reduce with the input and output forces becoming comparable to each other, although not perfectly overlapping. This deviation from perfect dynamic equilibrium is ascribed to the fact that the input strain gauge is located in proximity to the clamp, within the initially preloaded section of the bar, where vibrations can affect the measured signals. Additionally the interaction of the stress waves with the bars-collars-specimen connections may also affect slightly the assessment of the dynamic equilibrium conditions.

Fig. 10b illustrates the histories of direct stress and strain during loading. The average strain rate was calculated as the slope of the linear fit of the engineering strain-time history before the failure of the specimen. It is noted that the oscillation in the tensile stress history measured between 100  $\mu\text{s}$  and 200  $\mu\text{s}$  is not attributable to the dynamic response of the material but to the previously mentioned initial oscillation in the incident wave. This caused a transitory fluctuation and decrease of the applied strain rate, arrowed in Fig. 10b, which affected the tensile response. The stress history in Fig. 10b is representative of the mechanical response at the average longitudinal strain rate of  $113 \text{ s}^{-1}$  beyond 300  $\mu\text{s}$ .

As strains localise during deformation, engineering strains may differ from local strains. For this reason, the time history of the engineering strain (determined via image analysis), is compared to that of the local strain computed around the centre of the sample over a reduced length equal to 25% of the gauge length. It is clear, for this specific experiment, that nominal and local strains started to diverge only after the fracture of the specimen. This indicates that the assumption of homogeneity of the axial strain is valid up to fracture of the specimen under high-rate tensile

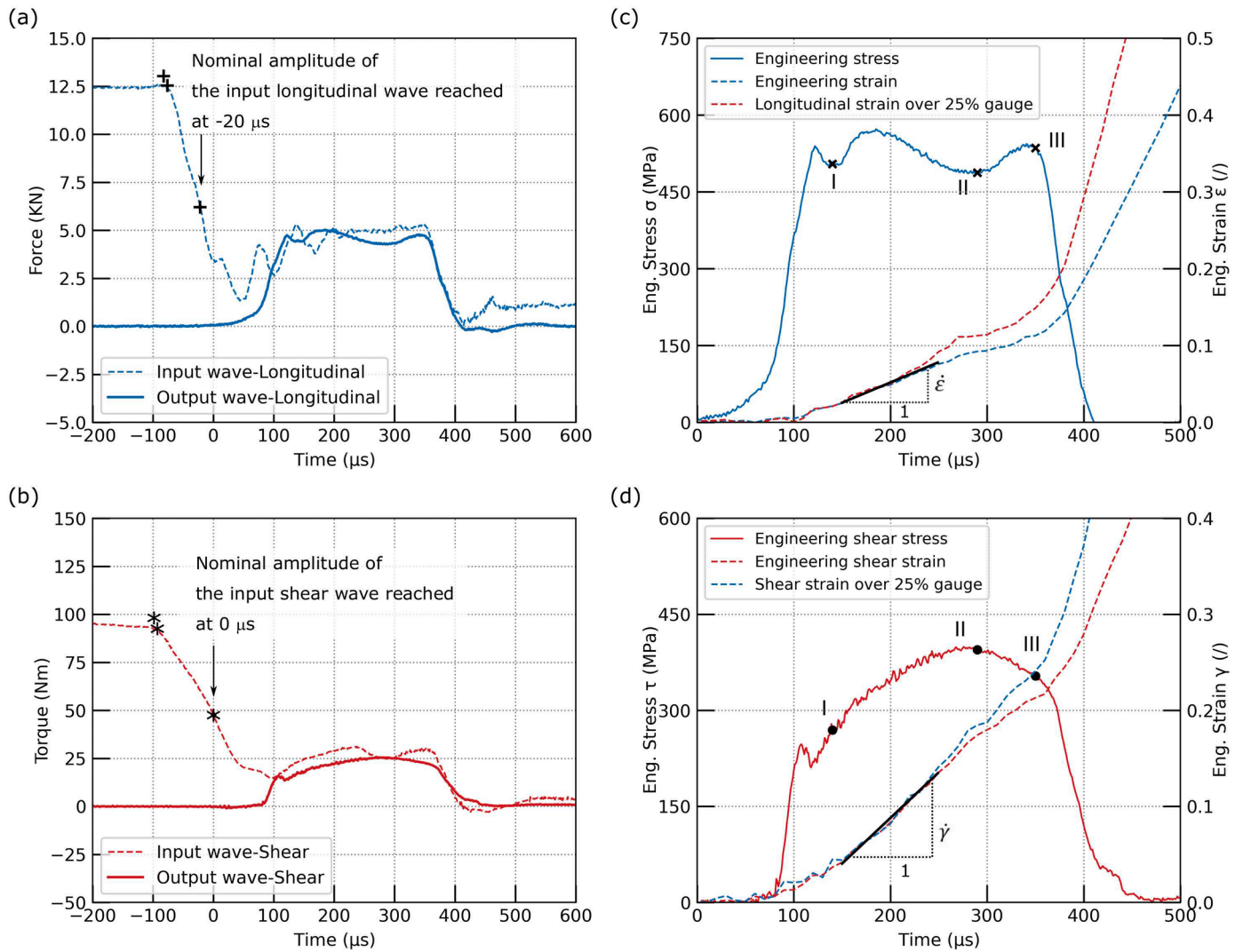


**Fig. 12.** Representative results from high-rate combined loading test (#HR6,  $\beta = 39.6^\circ$ ): (a), (b) assessment of dynamic equilibrium, (c) time histories of engineering direct stress, engineering direct strain and local longitudinal strain over 25% of the gauge length around the centre of the sample, (d) time histories of shear stress, engineering shear strain and local shear strain over 25% of the gauge length around the centre of the sample.

loading. The failure of the specimen corresponds to a dramatic increase in the strain as measured via the analysis of the high-speed camera footage. The measured strain to failure equal to 9.53% showed no marked increase compared to the quasi-static value, while the ultimate stress 747 MPa indicated pronounced strain rate sensitivity.

Representative high-rate responses in torsion loading conditions are depicted in Fig. 11. The drop in the initial level of the stored torque indicates the instant at which the incident wave starts loading the specimen (Fig. 11a). Thereafter, the shear input wave displayed only modest oscillations, approximately between 0 μs and 100 μs, thanks to the tight tolerance in the octagonal coupling between the bars and the specimen. After 200 μs the input and output forces become similar to each other, albeit perfectly overlapping only between 330 μs and 450 μs. This diversion from perfect dynamic equilibrium is attributed to the fact that the torsional input strain gauge is positioned within the preloaded section of the bar, where the release of the clamp may introduce moderate vibrations that can affect the measured signals.

Similarly to the case of dynamic tension, the shear strains homogenised along the whole gauge length are compared to the shear strains computed around the centre of the sample over a reduced length equal to 25% of the gauge length (Fig. 11b). It is visible that the curves start to diverge during plastic deformation with a difference of approximately 17% observed at the onset of fracture. This indicates that a localised

shear deformation zone develops around the centre of the sample since the early stages of plastic deformation, resulting in differences between nominal and local strains and strain rates.

As the specimen underwent strain hardening and then non-uniform deformation, the slope of the shear strain-time history decreased, approximately in correspondence to the ultimate shear stress point, 576 MPa. The average shear strain rate was calculated as the constant slope of the strain-time history before reaching the ultimate stress point. The strain rate sensitivity in torsion loading manifested as a significant increase of the ultimate stress, while no marked change of strain to failure.

Representative results from high-rate combined tension-torsion loading, where tension predominated ( $\beta = 39.6^\circ$ ), are presented in Fig. 12. The input tensile wave displays oscillations between 0 μs and 200 μs (Fig. 12a), attributed to the harsh release of the tensile elastic energy stored by the clamp. These fluctuations cease beyond 200 μs, where input and output force appear to be in reasonable agreement despite not perfectly superimposed. It is also evident, presumably because of different release mechanisms of the stored tensile and torsional energies, that the torsional input wave appears smoother than the input force (Fig. 12b). The comparison of the dynamic histories of input and output torques shows the input torque oscillating around the output signal (Fig. 12b).

The achievement of not perfect dynamic equilibrium conditions is

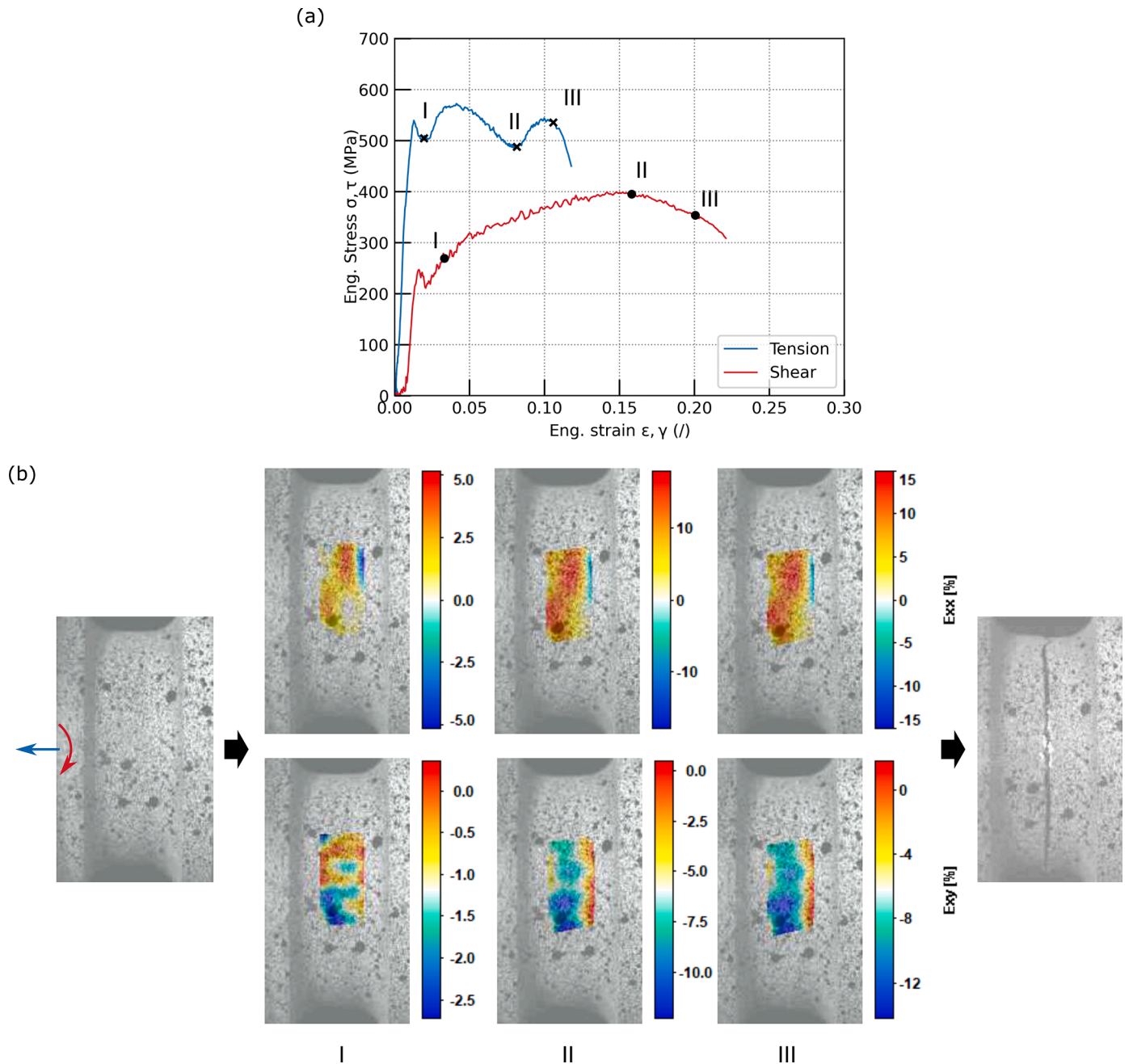


**Fig. 13.** (a) Engineering flow curves of CP-Ti under combined tension-torsion loading at high rate (#HR6,  $\beta = 39.6^\circ$ ); and (b) progressive deformation and failure mode.

explained by the fact that both the axial and shear input strain gauges are positioned in the segment of the input bar between the actuators and the clamp, where moderate vibrations may influence the measured signals, particularly in proximity to the clamp where the tensile gauge was placed. This is reasonable considering that the mechanisms of storage and fast release of concomitant torsional and tensile elastic energies may induce complex stress distributions in the clamped section. Additionally the interaction of the stress waves with the bars-collars-specimen connections and the octagonal couplings may also affect mildly the assessment of the dynamic equilibrium conditions. The approximately constant shear and tensile strain rates measured during combined tension-torsion loading experiment (Figs. 12c-d) corroborate the validity of the results herein presented.

Three instants synchronised in time (labelled as I, II and II in Fig. 12c-d) are marked on both the tensile and shear stress-time histories, to

analyse the development of the tensile and shear behaviours with regard to each other. Particularly, stage III marks the failure of the specimen, at which strain in both tension and shear increased dramatically upon the sudden drop of tensile and shear stresses, and a macroscopic crack became visible on the surface of the specimen. Stage III was synchronised in tension and shear, demonstrating the simultaneous failure. Similarly to the previous cases, the strains homogenised along the whole gauge length are compared to the strains computed around the centre of the sample over a reduced length equal to 25% of the gauge length (Fig. 12c-d). It is visible that nominal and local strains remain similar up to approximately 250  $\mu\text{s}$ , and then diverge until failure, with differences of approximately 27% and 12% for direct and shear strain at the onset of fracture.

The synchronisation of the longitudinal wave and shear wave is crucial in high-rate combined tension-torsion loading experiments. In all



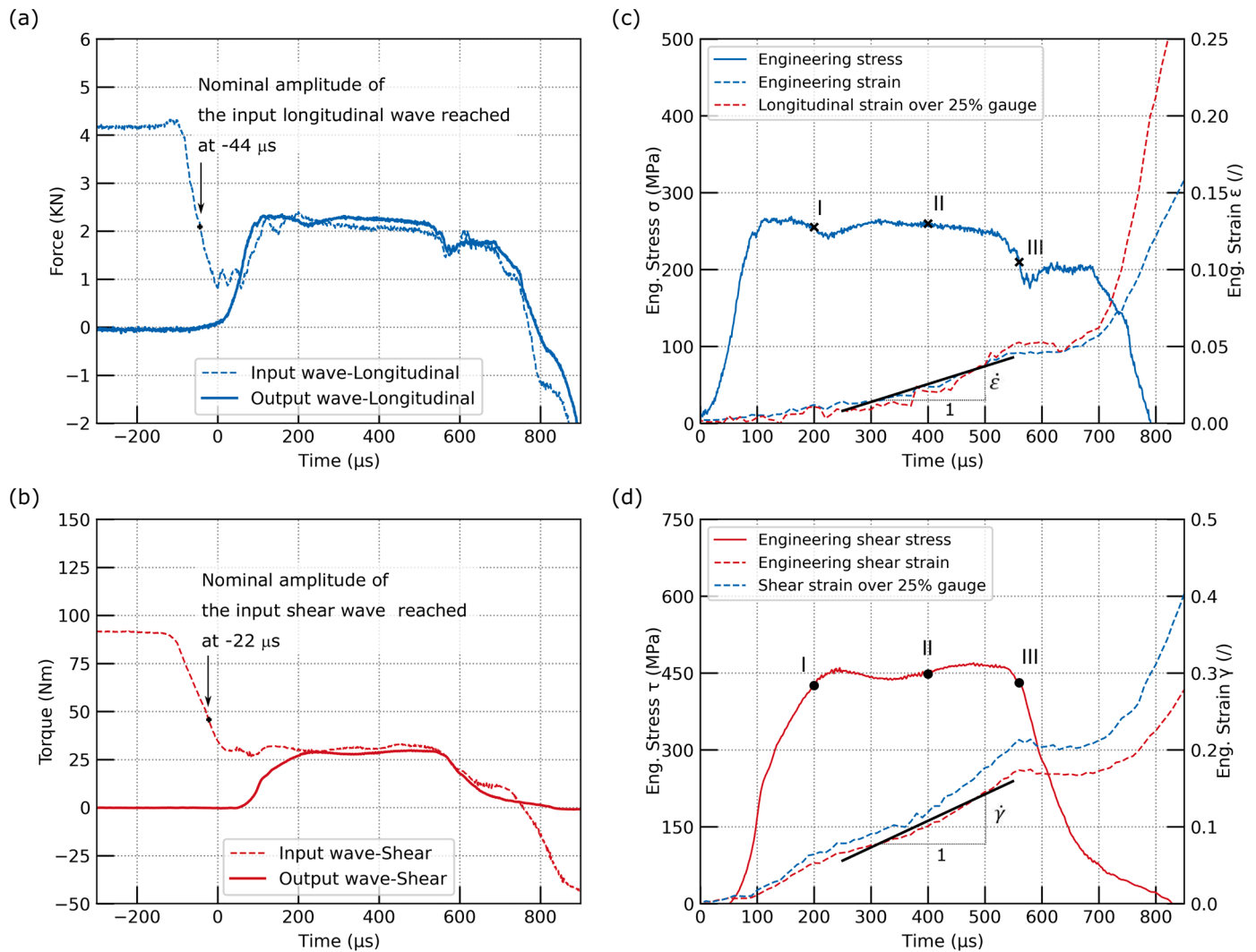


**Fig. 14.** Representative results from high-rate combined loading test (#HR8  $\beta = 18.3^\circ$ ): (a), (b) assessment of dynamic equilibrium, (c) time histories of engineering direct stress, engineering direct strain and local longitudinal strain over 25% of the gauge length around the centre of the sample, (d) time histories of shear stress, engineering shear strain and local shear strain over 25% of the gauge length around the centre of the sample.

the combined loading tests conducted, wave synchronisation was evaluated by comparing the instants at which the incident longitudinal and shear waves reach their nominal amplitudes, i.e., the instants when the measured stresses decrease to half of the stored preload magnitudes. Fig. 12a-b show that, for the specific case labelled as #HR6, the torsional wave reached its nominal amplitude  $20 \mu$ s later than the longitudinal wave (points \* and + in Fig. 12a-b). It is also noted that, plausibly due to the different releasing mechanisms of the stored tensile and torsional energies, the incident torque starts rising slightly earlier than the axial load (points \*\* and ++ in Fig. 12a-b). Therefore, it is clear that wave synchronisation was satisfied somewhere during the rise time of both waves, i.e., between \*/+ and \*\*/++ in Fig. 12. A time difference about  $10 \mu$ s between the arrival of the longitudinal and shear waves upon the specimen was reported in [33]. It is however important to mention that synchronised arrival of the waves in tension and shear does not necessarily mean synchronised deformation, which depends on the plastic stress wave velocities of the materials under investigation and on their intrinsic mechanical properties, such as ductility. Strictly speaking, synchronised arrival of longitudinal and shear waves, and synchronised deformation in tension and shear, can never be fulfilled in the combined tension-torsion experiment using a single clamp, due to the nature of the distinct wave speeds. Synchronised deformation, particularly for ductile materials, remains a challenge in combined tension-torsion

experimentation at high rates of strain. A possible approach could be separating the waves and timing their arrival upon the specimen in accordance with the direct and shear plastic wave velocities and deformation of the material.

The time histories of the nominal stress and strain in tension and shear were then combined to depict the tensile and shear flow curves in Fig. 13a. The tensile stress-strain curve exhibits some oscillations likely associated with the abrupt release of the stored elastic tensile energy discussed above. The shear curve exhibited the classical characteristics of ductile materials, with a linear elastic deformation phase and yielding, followed by a typical plastic flow phase featuring strain hardening, ultimate stress point and then localised deformation and macroscopic failure of the specimen. Contours of the tensile and shear strains measured from DIC analysis at the three stages I, II, and III are presented in Fig. 13b. As tension dominated in this combined loading case, the final fracture was located in the middle of the gauge section perpendicularly to the axial load. The strain field remained approximately homogeneous up to fracture initiation.

Results of another representative combined loading test in which shear predominated ( $\beta = 18.3^\circ$ ) are shown in Fig. 14. Dynamic equilibrium in tension was achieved thoroughly during the deformation of the sample (Fig. 14a). The dynamic torques measured on the input and output ends of the specimen show a certain discrepancy at early loading

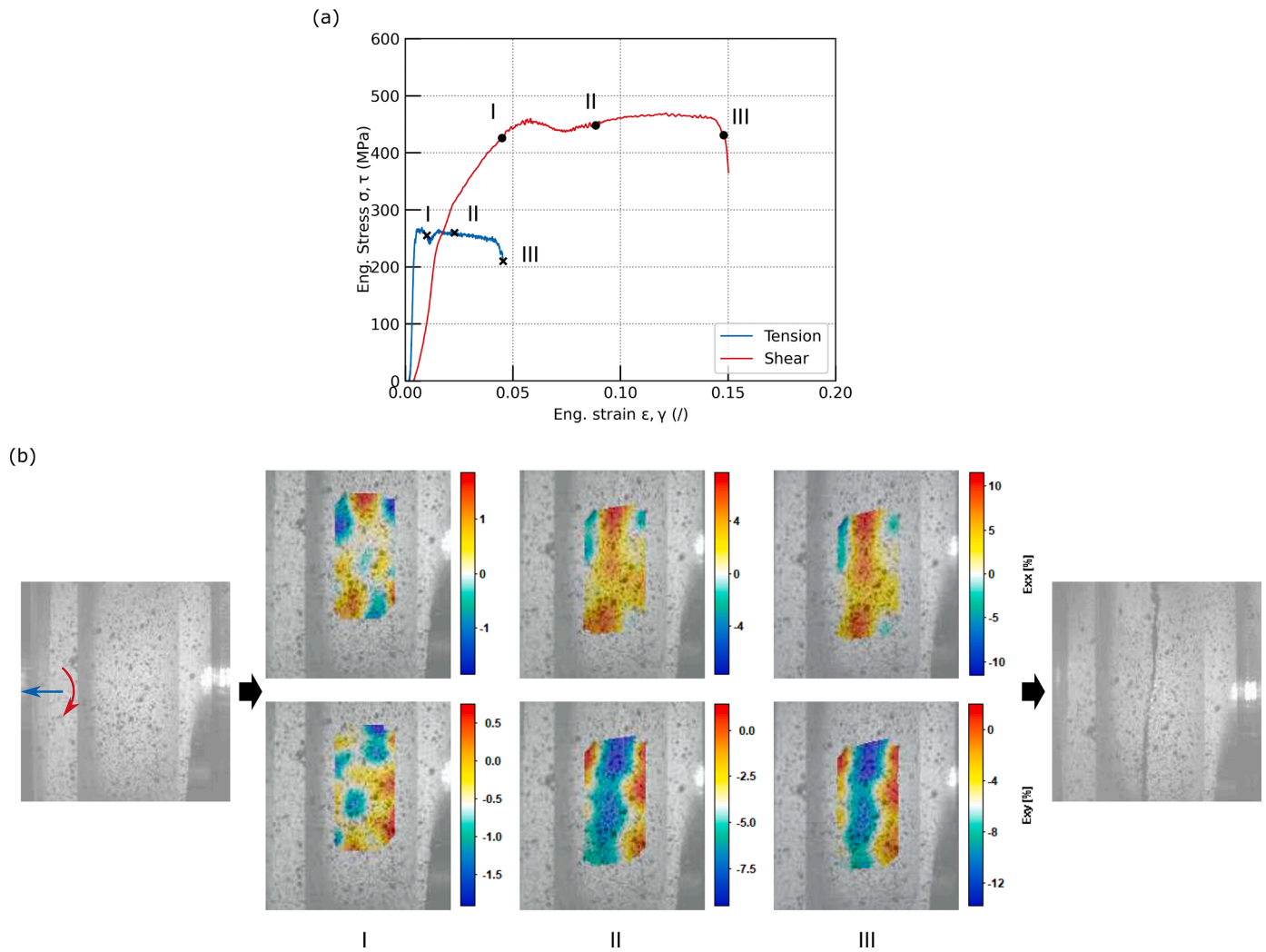


**Fig. 15.** (a) Engineering stress-strain curves of CP-Ti subjected to combined tension-torsion loading at high rate (#HR8,  $\beta = 18.3^\circ$ ); and (b) progressive deformation and failure mode.

stages, but dynamic equilibrium was attained later during plastic deformation as the shear wave propagated back and forth within the specimen (Fig. 14b). Synchronisation of the longitudinal wave and the shear wave was also verified with respect to the instant at which they reached their nominal amplitude, with a time difference of 22  $\mu$ s. Similarly to the previous cases, the strains homogenised along the whole gauge length are compared to the strains computed over a reduced length equal to 25% of the gauge length around the centre of the sample (Fig. 14c-d). It is evident that the assumption of homogeneity of the axial strain is valid up to failure while the shear strain curves start to diverge at the inception of plastic deformations with a difference of approximately 20% observed at the onset of failure. The histories of the tensile and shear strains illustrate an approximately constant strain rate loading up to the macroscopic failure of the specimen (stage III). The simultaneous failure in tension and shear was also demonstrated by the synchronised drop of the stresses and the concurrent swift increase of strain. Similar to the previous loading cases, the three representative stages are marked on the tensile and shear flow curves presented in Fig. 15, along with the corresponding strain contours. A certain strain localisation was observed between stages II and III, which eventually evolved into a macroscopic crack and the failure of the specimen across the gauge section. It is noted that the final fracture was not perfectly normal to the axial load but meandered along the circumference due to the prevailing shear for  $\beta = 18.3^\circ$ .

The high-rate behaviour of CP-Ti over a wide range of biaxial loading

angles is summarised in Fig. 16. The flow curves in tension and shear are presented in Fig. 16a and b, respectively. The black curve corresponds to tension loading ( $\beta = 90^\circ$ ), while the red curves correspond to pure shear ( $\beta = 0^\circ$ ). The curves in between represent different combinations of tension-torsion loads, in which the blue toned curves indicate the tension-dominated combinations while the orange toned ones indicate shear-dominated conditions. It is shown that the ultimate tensile stress decreases as the shear is prevailing, and so does the ultimate shear stress when tension predominates over shear. The increasing stress triaxiality appears to have little influence on the tensile failure strain, but substantially reduces the shear strain to failure. The loading paths of the measured nominal strains and engineering stresses up to failure are depicted in Fig. 16c and d, respectively. The evolution of the overall normal strain and shear strain within the gauge section was nearly proportional. The fixed ratio between the shear strain over the normal strain during the whole deformation process is explained by the fact that nearly constant strain rate loading in tension or/and torsion were achieved during all high-rate tests. From this point of view a conventional Hopkinson bar experiment is conducted in a strain rate controlled manner.

Fig. 16d shows that the trajectories described by direct stress and shear stress appear convoluted due to oscillations in the stress waves and their different propagation velocities. To have a better understanding of the evolution of the stress trajectories with respect to the stress-strain curves, five points are marked in the flow stress curves (Fig. 16a-b)

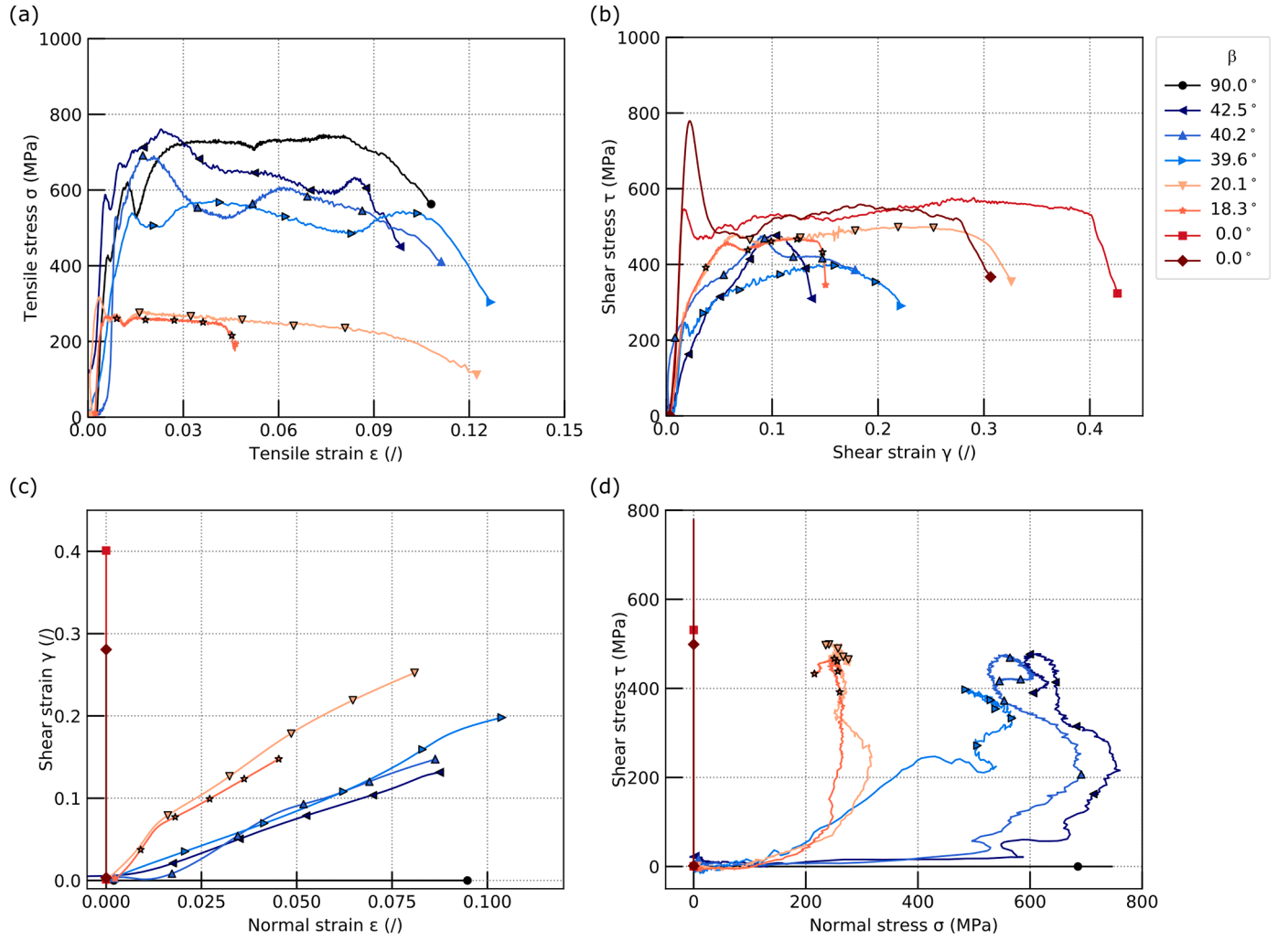


Fig. 16. Summary of the high-rate responses of CP-Ti measured from tension-torsion Hopkinson bar experiments: engineering stress-strain curves in (a) tension and (b) shear; loading trajectories of (c) engineering normal strain versus shear strain and (d) engineering normal stress versus shear stress.

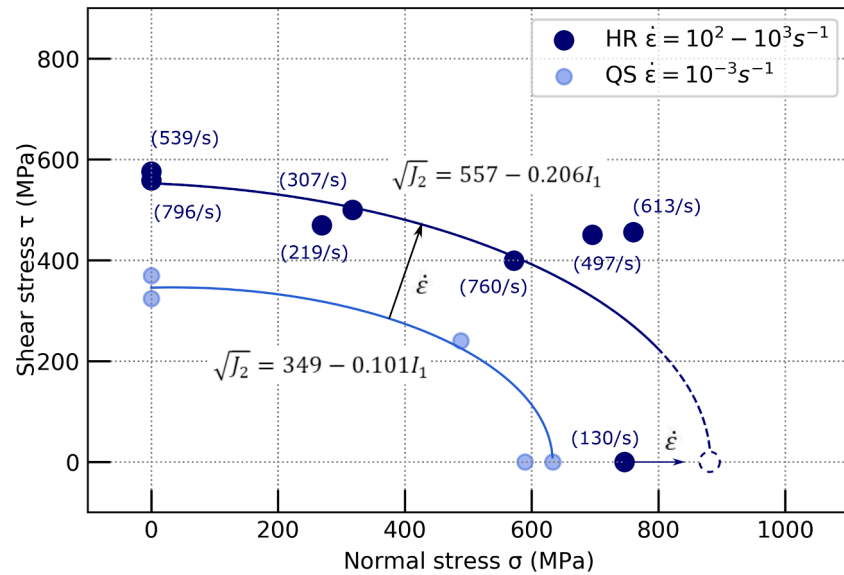
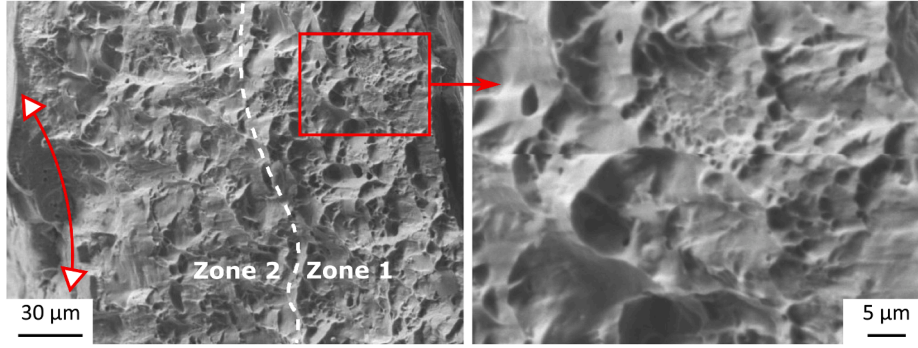
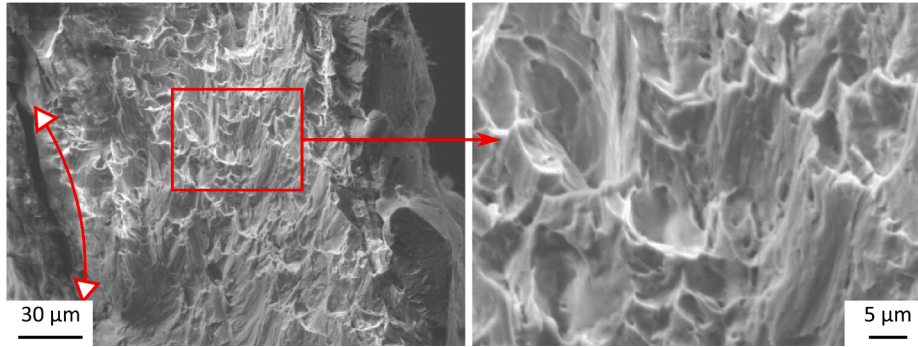


Fig. 17. Multiaxial failure locus of CP-Ti at quasi-static and dynamic rates of strain.



(a) Tension  $\beta = 90.0^\circ$ (b) Combined tension-torsion  $\beta = 49.5^\circ$ 

**Fig. 18.** Scanning electron micrographs of the fracture morphology of CP-Ti under quasi-static loading: (a) tension, and (b) tension-dominated combined loads. The double-headed curve denotes the inner wall of the tubular specimen.

and in the loading trajectories (Fig. 16c-d) under combined loading conditions. These five marks have the same shape as the symbol that identifies every curve in terms of  $\beta$  but have a black edge and are chosen such a way to divide the curves presented in Fig. 16a-b evenly in terms of strain. The last black-edged mark indicates the macroscopic fracture initiation.

It is noted that, while the marks are uniformly distributed along the trajectories of strain (Fig. 16c) they appear only in the final portion of each of the stress trajectories (Fig. 16d). This indicates that the segment of each stress path before the first mark is associated only with the early stages of loading. The initial portion of the stress trajectories appears to be nearly horizontal, regardless of the load being tension dominated ( $\beta$  approaching  $90^\circ$ ) or shear dominated ( $\beta$  approaching  $0^\circ$ ). This is due to the fact that the longitudinal wave propagation velocity is higher than the shear wave speed. Consequently the direct stress is always dominating in the initial phases of loading, approximately up to the yield point. The stress trajectories deviate from the initial almost horizontal trend when the direct stress nearly approaches the onset of plasticity under combined loading conditions. At this point, the shear stresses increase rapidly. It is worth specifying that the shear stress increases at an earlier stage for  $\beta = 39.6^\circ$  compared to the other combined loading cases due to the slightly longer rise time of the tensile transmitted pulse. During plastic deformation, in the region identified by the marks, the stress trajectories are governed by the ratio between the shear and the tensile flow stresses at the prescribed strain rate.

The proportion between normal and shear stresses is, for some loading cases ( $\beta = 18.3^\circ$  and  $\beta = 20.1^\circ$ ), less variable in the plastic region. However it is evident that this ratio is generally significantly affected by the oscillations present during dynamic loading and by the experimental scatter. This is apparent when comparing the stress trajectories measured for  $\beta = 39.6^\circ$ ,  $\beta = 40.2^\circ$  and  $\beta = 42.5^\circ$ , corresponding to approximately the same biaxial loading angle. It is therefore generally difficult to prescribe a stable ratio between direct and shear stresses during high rate combined tension-torsion experiments. A

reasonably steady proportion may be achievable only during plastic deformation, in absence of dynamic oscillations in the stress histories.

#### 4.3. Multiaxial failure stress envelope

We proceed to plot the ultimate stress of CP-Ti measured under various loading conditions in a normal versus shear stress space to evaluate the multiaxial failure locus of CP-Ti as the strain rate ranges from quasi static to high (Fig. 17). The circular markers in Fig. 17 are the experimental ultimate stresses under various combined loads, determined as the maximum measured engineering stresses in tension and shear. The early stress peak in experiment #HR3 ( $\beta = 0^\circ$  in Fig. 16b) was excluded because of the initial ringing in the stress strain data. The data points obtained in dynamic loading conditions are labelled in Fig. 17 with the average equivalent plastic strain rate measured during the experiments, defined as Eq. (6) assuming a state of plain strain in the circumferential direction and plane stress in the radial direction [37,38].

$$\dot{\epsilon}_{eq} = \sqrt{\frac{4}{3}\dot{\epsilon}^2 + \frac{1}{3}\dot{\gamma}^2} \quad (6)$$

where  $\dot{\epsilon}$  and  $\dot{\gamma}$  are the axial and shear strain rate respectively.

The Drucker-Prager (D-P) criterion (Eq. (7)) is employed to approximate the measured failure envelope:

$$\sqrt{J_2} = A + BI_1 \quad (7)$$

where,  $J_2$  denotes the second invariant of the deviatoric stress tensor, and  $I_1$  the first invariant of the stress tensor. It is worth emphasising that, as the D-P criterion is herein used to approximate the locus of the measured ultimate stresses,  $J_2$  and  $I_1$  represent the invariants corresponding to these values. The constants  $A$  and  $B$  are determined from the measured data via least square optimisation, herein implemented using a Trust Region Reflective algorithm [39]. Convergence of the optimisation is achieved in all cases with a tolerance of  $10^{-8}$ . The constants

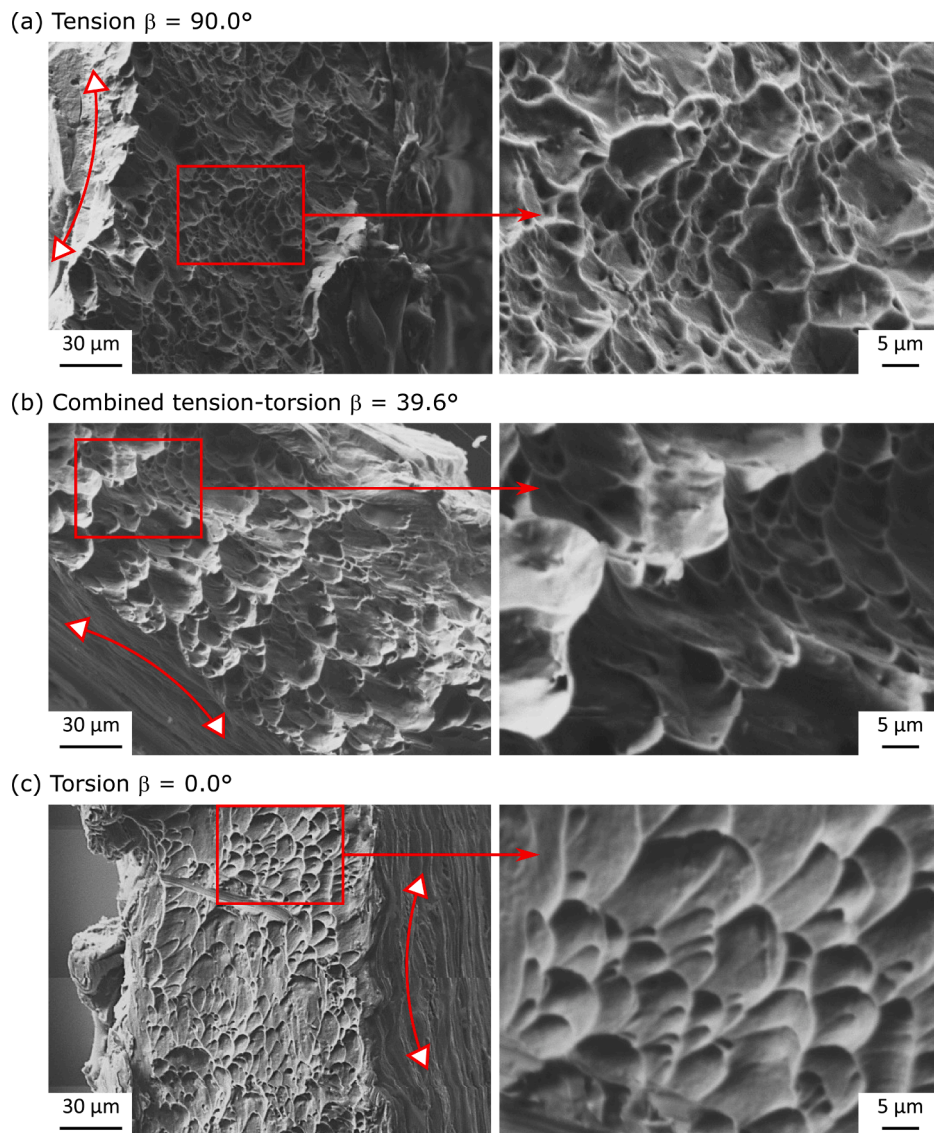


**Fig. 19.** Scanning electron micrographs of the fracture morphology of CP-Ti subjected to high-rate (a) tension, (b) tension-torsion combined load, and (c) torsion. The double-headed curves denote the inner wall of the tubular specimen.

that minimise the cost function are presented in Fig. 17.

The small value of the coefficient  $B$ ,  $-0.101$  at quasi-static rate and  $-0.206$  at dynamic strain rate, indicates a concentric expansion of the D-P failure envelope as the strain rate increases. The rate dependence of the multiaxial failure envelope is described by the coefficient  $A$  which varies from 349 to 557 with the increasing strain rate. The deviation of some of the data points from the high-rate envelope is explained by the slight variation of the strain rates measured in the dynamic loading regime. For instance, the data point obtained in dynamic uniaxial tension was obtained at a strain rate of  $113 \text{ s}^{-1}$ , which is lower compared to the other dynamic loading cases, as detailed in Table 2. Consequently, this point falls in between the D-P envelopes outlining the strength of the material at strain rates of approximately  $10^{-3} \text{ s}^{-1}$  and  $10^3 \text{ s}^{-1}$  respectively. This discrepancy can however be minimised by obtaining the envelopes at smaller strain rate intervals this way depicting the strain rate sensitivity of the material with higher resolution.

#### 4.4. Fracture morphology

The fracture mechanisms of CP-Ti at different stress states and strain rates was further investigated examining the fracture surfaces of the

samples by means of SEM imaging. The SEM micrographs were recorded using a Carl Zeiss Evo LS15 variable pressure scanning electron microscope. A Secondary electron detector (SE) was used for all the images, at a voltage of 15 kV with a working distance of 9.00 mm.

Fig. 18 illustrates the fracture surface characteristics of CP-Ti under quasi-static loading. The micrographs include a specimen that fractured under tension  $\beta = 90^\circ$  (Fig. 18a), and one under tension-dominated combined loading  $\beta = 49.5^\circ$  (Fig. 18b). As the quasi-static torsion specimens did not separate into two halves at fracture the failure surface for this case is not presented. The examination of the fracture surface of the tensile specimen revealed two different zones which underwent different plastic deformation mechanisms (Fig. 18a). One zone is characterised by the formation of equiaxed dimples (zone 1), typical of a ductile fracture, while the other region is characterised by slip dominated plastic deformation (zone 2). A higher magnification of the ductile tearing of voids is shown in the magnified image. Zone 2 presents a lower occurrence of voids, shallower, intercalated with regions where slip appears to be the dominating plastic deformation mechanism. The fracture morphology of the tension-torsion loaded specimen (Fig. 18b) displays two main different plastic deformation mechanisms. One represented by void formation, growth and coalescence, and the other one

by slip. The dimples appear teared, indicating the presence of shear stress, with uniform size and orientated in the same direction, at an angle of approximately  $45^\circ$  from the radial direction. The slip regions appear larger than the voids. These slip regions may have eased the accommodation of plastic deformation, leading the specimen to exhibit less ductility before fracture.

The fracture surfaces of the dynamically loaded specimens are shown in Fig. 19. The fractographs, at two different magnifications, include three representative stress states: tension (Fig. 19a), tension-torsion combined load with  $\beta = 39.6^\circ$  (Fig. 19b), and torsion (Fig. 19c). All SEM images clearly reveal dimples on the fracture surface, indicative of ductile fracture, regardless of the stress state. The fracture surface of the high-rate tensile specimen ( $\beta = 90^\circ$  Fig. 19a) shows a uniformly ordered array of equiaxed dimples. Few larger dimples with subdimples coalesced inside can be observed in the higher magnification image. The combined loaded specimen of biaxial loading angle  $\beta = 39.6^\circ$  (Fig. 19b), displays a fracture surface containing larger dimples elongated in circumferential direction. The elongated shape is attributed to the shear deformation. Subdimples clusters can be distinguished at the boundary of the large dimples in the higher magnification fractography. The fracture surface of the high-rate torsion specimen, ( $\beta = 0^\circ$  Fig. 19c) displays groups of elongated but shallow dimples, in contrast to the tensile specimen (Fig. 19a) which features a fracture surface with a high density of small but deep dimples. The influence of the stress state on the fracture surface is also clearly shown in the combined loading case  $\beta = 39.6^\circ$  (Fig. 19b), featuring a mixture of dense and deep but also larger elongated dimples. In general, larger and elongated dimples are observed as the biaxial angle decreases, i.e., as the shear load dominates. Larger and more elongated dimples indicate a higher fracture strain [40]. Hence the characteristics of the fracture surfaces agree with the measured macroscopic mechanical behaviours of CP Ti under investigation as larger failure strains were measured when torsion dominated during combined loading.

## 5. Conclusion

The failure stress locus of commercially pure titanium (CP-Ti) subjected to arbitrary combinations of tension and shear loads at low and high rates of strain was determined from direct experimental measurements. The failure envelope was analysed over a wide range of stress states including pure shear, shear-dominated combined tension-shear, tension-dominated combined tension-shear, and tension. The analyses of the loading paths show that direct and shear strain were nearly proportional during deformation. The Drucker-Prager criterion was employed to approximate the stress envelope and to quantify its rate sensitivity. The material was evidently rate dependant as its failure stress locus expands concentrically with the strain rate increasing from  $10^{-3}$  to  $10^3 \text{ s}^{-1}$ .

Quasi-static experiments were carried out using a universal screw-driven machine. Experiments at high strain rate were conducted on a novel split Hopkinson tension-torsion bar (TTHB) apparatus capable of implementing an arbitrary combination of tension and torsion loads. Synchronisation of the longitudinal and shear waves upon loading the specimen was achieved during all experiments. The wave propagation was elaborated by means of  $x$ - $t$  and  $v$ - $t$  diagrams to understand the evolution of incident, reflected, and transmitted waves during dynamic experiments. The analyses of dynamic experiments on CP-Ti demonstrated the ability of the TTHB apparatus to achieve dynamic equilibrium and constant strain rate conditions during combined tension-torsion loading.

Further research will focus on the following aspects: (i) post-mortem analysis to reveal the effect of stress triaxiality on fracture surface and microstructure within the damage zone, and (ii) controlled dynamic axial and shear loading sequence to assess the sensitivity of engineering materials to the applied high-rate loading path.

The key value of the findings presented in this paper lies on the

capability of the proposed TTHB apparatus to populate the failure stress locus of aerospace materials directly from experimental measurements. This allows a better assessment of the existing and novel failure/yielding criteria and serves as constitutive model input for the optimal design of engineering structures subjected to impact loading.

## CRediT authorship contribution statement

**Yuan Xu:** Conceptualization, Methodology, Investigation, Formal analysis, Visualization, Writing – original draft. **Maureen Aceves Lopez:** Formal analysis, Visualization. **Junyi Zhou:** Investigation. **Lukasz Farbaniec:** Writing – review & editing. **Sophoclis Patsias:** Project administration. **Duncan Macdougall:** Writing – review & editing. **Julian Reed:** Resources. **Nik Petrinic:** Funding acquisition. **Daniel Eakins:** Resources. **Clive Siviour:** Resources. **Antonio Pellegrino:** Conceptualization, Supervision, Funding acquisition, Project administration, Writing – review & editing.

## Declaration of Competing Interest

The authors declare that they have no known competing financial interests or personal relationships that could have appeared to influence the work reported in this paper.

## Acknowledgement

The authors would like to thank Rolls-Royce plc and the EPSRC for the support under the Prosperity Partnership Grant\Cornerstone: Mechanical Engineering Science to Enable Aero Propulsion Futures, Grant Ref: EP/R004951/1. The authors are grateful to Mr. S. Carter, Mr. J. Fullerton, Mr. D. Robinson and Mr. P. Tantrum for their assistance with manufacturing, and Mrs. K. Bamford for her immense help with procurement. The authors would also like to thank Dr. D. Townsend for the stimulating discussions during the experimentation.

## References

- [1] Boyer RR. An overview on the use of titanium in the aerospace industry. *Mater Sci Eng A* 1996;213(1–2):103–14. [https://doi.org/10.1016/0921-5093\(96\)10233-1](https://doi.org/10.1016/0921-5093(96)10233-1).
- [2] Chen Q, Thouas GA. Metallic implant biomaterials. *Mater Sci Eng R* 2015;87:1–57. <https://doi.org/10.1016/j.mser.2014.10.001>.
- [3] Gong Y, Yang ZG, Yuan JZ. Failure analysis of leakage on titanium tubes within heat exchangers in a nuclear power plant. Part II: mechanical degradation. *Mater Corros* 2012;63:18–28. <https://doi.org/10.1002/maco.201106190>.
- [4] Hussam EFS. Finite element simulation of hip joint replacement under static and dynamic loading. Doctoral dissertation. Dublin City University; 2000.
- [5] Shalaby HM, Al-Mazeedi H, Gopal H, Tanoli N. Failure of titanium condenser tube. *Eng Fail Anal* 2011;18(8):1990–7. <https://doi.org/10.1016/j.engfailanal.2011.05.008>.
- [6] Ma TH, Chang L, Guo S, Kong LR, He XH, Zhou CY. Comparison of multiaxial low cycle fatigue behavior of CP-Ti under strain-controlled mode at different multiaxial strain ratios. *Int J Fatigue* 2020;140:105818. <https://doi.org/10.1016/j.ijfatigue.2020.105818>.
- [7] Hopkinson B. A method of measuring the pressure produced in the detonation of high explosives or by the impact of bullets. *Philos T R Soc A* 1914;213:437–56.
- [8] Kolsky H. An investigation of the mechanical properties of materials at very high rates of loading. *Proc Phys Soc* 1949;62:676–700.
- [9] Field JE, Walley SM, Proud WG, Goldrein HT, Siviour CR. Review of experimental techniques for high rate deformation and shock studies. *Int J Impact Eng* 2004;30(7):725–75.
- [10] Gama BA, Lopatnikov SL, Gillespie JW. Hopkinson bar experimental technique: a critical review. *Appl Mech Rev* 2004;57(4):223–50.
- [11] Gerlach R, Kettenbeil C, Petrinic N. A new split Hopkinson tensile bar design. *Int J Impact Eng* 2012;50:63–7.
- [12] Chichili DR, Ramesh KT, Hemker KJ. The high-strain-rate response of alpha-titanium: experiments, deformation mechanisms and modeling. *Acta Mater* 1998;46(3):1025–43.
- [13] Gurao NP, Kapoor R, Suwas S. Deformation behaviour of commercially pure titanium at extreme strain rates. *Acta Mater* 2011;59(9):3431–46.
- [14] Li Q, Xu YB, Bassim MN. Dynamic mechanical behavior of pure titanium. *J Mater Process Tech* 2004;155:1889–92.
- [15] Kailas SV, Prasad YVRK, Biswas SK. Microstructural features of flow. *Metall Mater Trans A* 1993;24:2513–20.



- [16] Kailas SV, Prasad YVRK, Biswas SK. Influence of initial texture on the microstructural instabilities during compression of commercial  $\alpha$ -titanium at 25 °C to 400 °C. *Metall Mater Trans A* 1994;25(7):1425–34.
- [17] Nemat-Nasser S, Guo WG, Cheng JY. Mechanical properties and deformation mechanisms of a commercially pure titanium. *Acta Mater* 1999;47(13):3705–20.
- [18] Harding J. The temperature and strain rate sensitivity of  $\alpha$ -titanium. *Arch Mech* 1975;27:715–32.
- [19] Huang W, Zan X, Nie X, Gong M, Wang Y, Xia Y. Experimental study on the dynamic tensile behavior of a polycrystal pure titanium at elevated temperatures. *Mater Sci Eng A* 2007;443(1–2):33–41.
- [20] Yuan JM, Shim VPW. Tensile response of ductile  $\alpha$ -titanium at moderately high strain rates. *Int J Solids Struct* 2002;39(1):213–24.
- [21] Tsao MC, Campbell JD. Plastic shear properties of metals and alloys at high strain rates. Oxford, UK: Oxford University, Department of Engineering Science; 1973.
- [22] Randall M, Campbell J. Dynamic plasticity under combined stresses: the development and use of a medium rate tension-torsion machine. University of Oxford; 1972.
- [23] Chen H, Li F, Zhou S, Li J, Zhao C, Wan Q. Experimental study on pure titanium subjected to different combined tension and torsion deformation processes. *Mater Sci Eng A* 2017;680:278–90.
- [24] Smirnov I, Polyakov A, Sudenkov Y. Strength and fracture of ultrafine-grained titanium Grade 4. *Procedia Struct Integr* 2017;6:196–200.
- [25] Polyakov AV, Semenova IP, Raab GI, Sitdikov VD, Valiev RZ. Peculiarities of ultrafine-grained structure formation in Ti Grade-4 using ECAP-Conform. *Rev Adv Mater Sci* 2012;31(1):78–84.
- [26] Gilat A, Cheng CS. Testing with the torsional split Hopkinson bar at strain rates above 10,000 1/s. *WIT. Trans Built Environ* 1998;35:549–58.
- [27] Macdougall DAS, Harding J. The measurement of specimen surface temperature in high-speed tension and torsion tests. *Int J impact Eng* 1998;21(6):473–88.
- [28] Zhang L, Townsend D, Petrinic N, Pellegrino A. Measurement of pure shear constitutive relationship from torsion tests under quasi-static, medium, and high strain rate conditions. *J Appl Mech* 2021;8(12):121003.
- [29] Pan B, Lu Z, Xie H. Mean intensity gradient: an effective global parameter for quality assessment of the speckle patterns used in digital image correlation. *Opt Lasers Eng* 2010;48:469–77.
- [30] Quino G, Chen Y, Ramakrishnan KR, Martínez-Hergueta F, Zumpano G, Pellegrino A, Petrinic N. Speckle patterns for DIC in challenging scenarios: rapid application and impact endurance. *Meas Sci Technol* 2021;32:015203.
- [31] Gilat A, Cheng CS. Torsional split Hopkinson bar tests at strain rates above 104 s<sup>-1</sup>. *Exp Mech* 2000;40(1):54–9.
- [32] Pope DP, Vreeland Jr T, Wood DS. Machine for producing square torsion pulses of microsecond duration. *Rev Sci Instrum* 1964;35:1351–5.
- [33] Lewis JL, Goldsmith W. The dynamic fracture and prefracture response of compact bone by split Hopkinson bar methods. *J Biomech* 1975;8:27–40.
- [34] Kolsky H. Stress waves in solids. Oxford: Clarendon Press; 1953.
- [35] Xu Y, Farbaniec L, Siviour C, Eakins D, Pellegrino A. The development of split Hopkinson tension-torsion bar for the understanding of complex stress states at high rate. In: Lamberson L, Mates S, Eliasson V, editors. *Dynamic behavior of materials, Volume 1. Conference proceedings of the society for experimental mechanics series*; 2021. p. 89–93.
- [36] Zhang L, Townsend D, Petrinic N, Pellegrino A. Measurement of pure shear constitutive relationship from torsion tests under quasi-static, medium and high strain rate conditions. *J Appl Mech* 2021;1–26. <https://doi.org/10.1115/1.4052001>.
- [37] Papasidero J, Doquet V, Mohr D. Determination of the effect of stress state on the onset of ductile fracture through tension-torsion experiments. *Exp Mech* 2014;54:137–51.
- [38] Faleskog J, Barsoum I. Tension-torsion fracture experiments - Part I: experiments and a procedure to evaluate the equivalent plastic strain. *Int J Solids Struct* 2013;50(25–26):4241–57.
- [39] Branch MA, Coleman TF, Li Y. A subspace, interior, and conjugate gradient method for large-scale bound-constrained minimization problems. *SIAM J Sci Comput* 1999;21(1):1–23.
- [40] Verleysen P, Peirs J. Quasi-static and high strain rate fracture behaviour of Ti6Al4V. *Int J Impact Eng* 2017;108:370–88.